Basin-scale interaction between post-LGM faulting and morpho-sedimentary processes in the S. Eufemia Gulf (Southern Tyrrhenian Sea)

E. Martorelli [a,*], D. Casalbore [b], A. Bosman [a], F. Pepe [c], M. Corradino [c,d], R. de Nardis [e], C. Monaco [d,f,g], A. Sposato [a]

[a] CNR-IGAG, Rome, Italy
[b] Dipartimento di Scienze della Terra, Sapienza Università, Rome, Italy
[c] Dipartimento di Scienze della Terra e del Mare, Università di Palermo, Palermo, Italy
[d] Dipartimento di Scienze Biologiche, Geologiche e Ambientali, Università di Catania, Catania, Italy
[e] Dipartimento di Scienze della Terra, Università di Chieti, Chieti, Italy
[f] CRUST-DiSTAR, Centro inter Universitario per L'analisi SismoTettonica Tridimensionale con Applicazioni Territoriali, Università G. d'Annunzio, Chieti Scalo, Italy
[g] Istituto Nazionale di Geofisica e Vulcanologia, Osservatorio Etneo, Catania, Italy

ARTICLE INFO

ABSTRACT

The integrated interpretation of high-resolution multibeam bathymetry, seismic profiles and backscatter data in the S. Eufemia Gulf (SEG; Calabro-Tyrrhenian continental margin, south-eastern Tyrrhenian Sea) documents the relationship between postglacial fault activity and morpho-sedimentary processes. Three systems of active normal faults that affect the seafloor or the shallow subsurface, have been identified: 1) the S. Eufemia fault system located on the continental shelf with fault planes mainly oriented N26E-N40E; 2) the offshore fault system that lies on the continental slope off Capo Suvero with fault planes mainly oriented N28E-N60E; 3) the Angitola Canyon fault system located on the seafloor adjacent to the canyon having fault planes oriented N60E-N85E. The faults produce a belt of linear escarpments with vertical displacement varying from a few decimeters to about 12 m. One of the most prominent active structures is the fault F1 with the highest fault length (about 9.5 km). Two main segments of this fault are identified: a segment characterised by seafloor deformation with metric slip affecting Holocene deposits; a segment characterised by folding of the seafloor. A combined tectono-stratigraphic model of an extensional fault propagation fold is proposed here to explain such different deformation.

In addition to the seabed escarpments produced by fault deformation, in the SEG, a strong control of fault activity on recent sedimentary processes is clearly observed. For example, canyons and channels frequently change their course in response to their interaction with main tectonic structures. Moreover, the upper branch of the Angitola Canyon shows straight flanks determined by fault scarps. Tectonics also determined different sediment accumulation rates and types of sedimentation (e.g., the accumulation of hanging wall turbidite deposits and the development of contourite deposits around the Maida Ridge). Furthermore, the distribution of landslides is often connected to main fault scarps and fluids are locally confined in the hanging wall side of faults and can escape at the seabed, generating pockmarks aligned along their footwall.

1. Introduction

The analysis of geomorphological and sedimentary records of tectonically active continental margins is often difficult due to the complex interplay of various processes, such as tectonics, climate, eustatic sea-level changes, slope instability, along-slope bottom currents, erosion patterns and sediment supply from upland source areas (e. g., Allen, 2008; Ercilla et al., 2008; Rebesco and Camerlenghi, 2008; Allen and Allen, 2013; Pickering and Hiscott, 2016; García et al., 2020). Tectonics tends to exert a predominant influence on the stratigraphic

---

architecture of margins and basins fill at both local and regional scales, affecting, for example, the distribution of depositional and erosional systems (e.g., submarine canyons; Laursen and Normark, 2002; Le Dantec et al., 2010; Micallef et al., 2014) and the occurrence of instability phenomena (Watson et al., 2020). At the local scale, features typically resulting from the tectonic activity are abrupt changes in the canyon course and sinuosity, offset of the canyon axis, knickpoints in longitudinal profiles and flanks-head geometry (Micallef et al., 2014 and

references therein). Also, fault activity may determine a concentration of landslides (e.g., Watson et al., 2020; Kluesner et al., 2020) because it may represent either a predisposing condition (e.g., steep slopes) or a triggering factor (i.e., earthquakes) for slope instability (e.g., Piper et al., 1999; Geist, 2000; Tanyaş et al., 2019). Finally, faults often represent the main migration pathways for fluids, determining their seeping at the seabed and the formation of specific structures, such as pockmarks, mud volcanoes, carbonate mounds, etc. (Hovland and Judd, 1988).
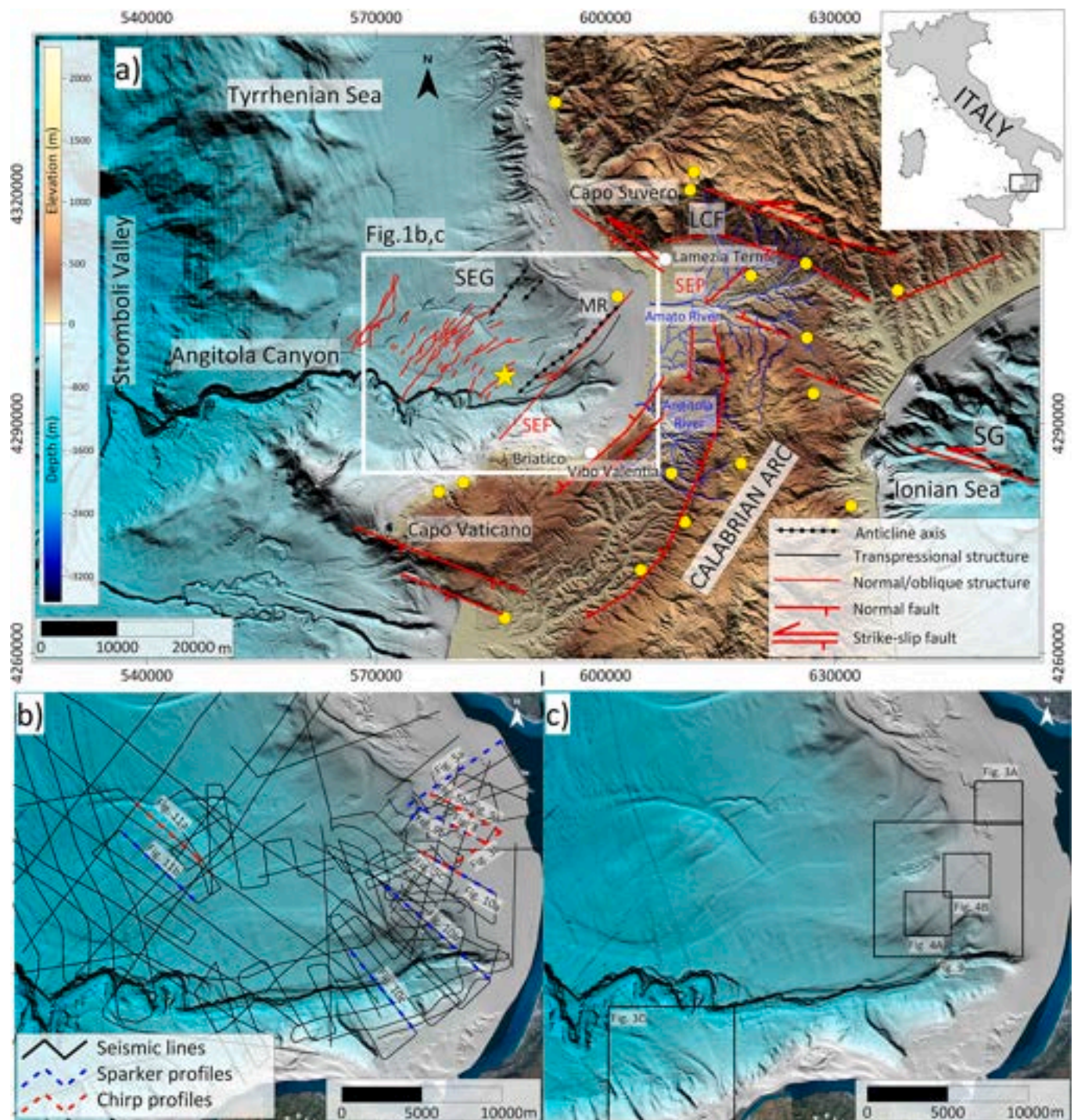

Fig. 1. a) Schematic tectonic sketch map of the S. Eufemia Gulf in the Tyrrhenian Sea (modified from Monaco and Tortorici, 2000; Brutto et al., 2016) and offshore (modified from Loreto et al., 2013; Del Ben et al., 2008). Yellow circles indicate Mw > 5 earthquakes from CPTI15 Catalogue (Rovida et al., 2022); the yellow star indicates the location of the 1905 epicentre. LCF: Lamezia-Catanzaro Fault; SEF: S. Eufemia Fault; SEG: S. Eufemia Gulf; SEP: S. Eufemia Plain; MR: Maida Ridge. b) High-resolution single-channel seismic track lines collected in the SEG. c) Location of the figures of the bathymetric features shown in the manuscript. (For interpretation of the references to color in this figure legend, the reader is referred to the web version of this article.)

The S. Eufemia Gulf (SEG, Fig. 1) is located in the central sector of the western Calabrian margin (south-eastern Tyrrhenian Sea), in the fore-arc region of the Tyrrhenian-Ionian subduction system (Fig. 1a). Central Calabria is a tectonically active area that was affected by strong earthquakes in historical times. Among these, the 1905 event of Mw 7.0 had its epicentre in the SEG (e.g., Galli and Molin, 2009; Tertulliani and Cucci, 2009; Rovida et al., 2020; Fig. 1). Main tectonic structures were detected in the Plio-Quaternary deposits of the SEG, and recently described by Loreto et al. (2013, 2015), Brutto et al. (2016) and Corradino et al. (2021). In particular, Loreto et al. (2013) identified a NNE-SSW trending normal fault (named the S. Eufemia fault) possibly linked to the 1905 earthquake. Furthermore, Corradino et al. (2021) distinguished between shallow active normal faults, and deep blind reverse faults, potentially associated with large earthquakes. Also, among these deep faults, they detected the possible seismogenic source of the 1905 seismic event. However, a comprehensive analysis of the shallow active faults and their influence on sedimentation and morpho-sedimentary dynamic is still lacking.

Due to the presence of various morpho-sedimentary features and high accumulation rates of post-Last Glacial Maximum (LGM) deposits, the SEG represents a suitable area to investigate the geomorphic and sedimentary response to active faults formed offshore. This study aims: 1) to document the geometry of active faults formed in the SEG and their post-LGM activity; 2) to understand the interplay between active tectonic deformation and morpho-sedimentary processes; and 3) to recognise the role of non-tectonic factors influencing margin shaping. The comprehension of these topics is significant to improve the knowledge of active faults of the western Calabrian margin and to provide new insights into the field of tectonic geomorphology and sedimentology, which represent still evolving disciplines in marine studies (e.g., Burbank and Anderson, 2001; Leeder, 2011). To reach this aims we analysed high-resolution multibeam bathymetry and side scan sonar data integrated with high-resolution 2-D seismic profiles and remote operated vehicle videos.

2. Geological setting

The SEG is located in the Tyrrhenian offshore of the Calabrian Arc (Fig. 1a), an allochthonous segment of the Apennine Maghrebian fold and thrust belt. Its arcuate shape is due to the southeastward migration of the Apennine belt and its diachronous collision with the Apulian and Hyblean foreland to the north and south, respectively (Mattei et al., 2007). The migration occurred along NW-SE to WNW-ESE-trending regional strike-slip fault systems that fragmented the Calabrian Arc into NW-SE elongated blocks. The main strike-slip fault systems are the Pollino and Sangineto systems to the north and their offshore prolongations (Monaco et al., 1998; Van Dijk et al., 2000; Ferranti et al., 2009; De Ritis et al., 2019); the Lamezia-Catanzaro line in the central sector (Tansi et al., 2007; Pirrotta et al., 2021) and its offshore prolongation (S. Eufemia and Squillace gulfs, Fig. 1a; Del Ben et al., 2008; Corradino et al., 2021); the Tindari line in the north-eastern Sicily (Cultrera et al., 2017; Barreca et al., 2019). Other NNW-SSE strike-slip fault systems affected the Tyrrhenian and Ionian offshore of the Calabrian Arc (i.e., Paola anticline, Squillace basin and Amendolara ridge; Corradino et al., 2020, 2023; Ferranti et al., 2014, respectively). Seismicity with severe earthquakes (Mw > 6) affected the Calabrian Arc and the SEG in the last centuries, related both to the activity of the transversal strike-slip fault systems and to the reactivation of normal faults bounding Plio-Quaternary longitudinal basins located along the Tyrrhenian side (Fig. 1, Monaco and Tortorici, 2000; Jacques et al., 2001; Basili et al., 2021).

The SEG is characterised by two km-thick Plio-Quaternary deposits, overlying deformed Miocene units (Trincardi et al., 1995; Milia et al., 2009; Loreto et al., 2013; Corradino et al., 2021). The continental shelf is 1–9 km wide and characterised by Plio-Pleistocene siliciclastic prograding units, mainly formed during lowstand and forced regressive

stages (Chiocci and Orlando, 1995). About 70 m-thick transgressive and highstand deposits were recognised within the depositional sequence formed since the Last Glacial Maximum (LGM; Chiocci et al., 1989; Martorelli et al., 2010a; Pepe et al., 2014), hereafter named Late Quaternary Depositional Sequence (LQDS). The continental slope is 3–4° steep and dissected by prominent ridges (e.g., the Maida Ridge, Corradino et al., 2021), faults scarps and erosive features (e.g., landslides scars and canyons, Loreto et al., 2013; Corradino et al., 2021). The main erosive structure is the Angitola Canyon (Fig. 1a) that develops from the outer shelf down to the Stromboli Valley (Gamberi and Marani, 2007). The ENE-WSW-oriented straight upper reach, followed by a meandering course, suggests that the Angitola Canyon is tectonically controlled (Loreto et al., 2013; Corradino et al., 2021).

The tectonic evolution of the SEG was divided in three stages (Corradino et al., 2021): 1) a Late Miocene extensional (or transtensional) stage, followed by 2) a right-lateral transpressional tectonic event during the Pliocene-Early Pleistocene (Gelasian) that caused the positive inversion of deep (>3 km) extensional tectonic features and the formation of NNE-SSW to NE-SW trending anticlines (e.g., the Maida Ridge), and 3) an Early Pleistocene-Recent left-lateral transtensional phase that led to the formation of shallow (<1.5 km) NNE-SSW oriented, high-angle normal to transtensional faults. Eastward, the SEG is bounded by the S. Eufemia Plain (SEP in Fig. 1a), a structural depression filled by a Plio-Quaternary sequence of marine to continental deposits (Tortorici et al., 2002). The plain is mostly floored by Late Pleistocene-Holocene conglomerate and sand deposits related to different generations of alluvial fans formed by a network of narrow and steep water courses (Ruello et al., 2017). In particular, the Amato and Angitola Rivers flow through the plain's central and southern sectors (Fig. 1a). To the North, the S. Eufemia Plain is bounded by the Lamezia–Catanzaro Fault System (LCF in Fig. 1a), characterised by a left-lateral component of motion along the WNW–ESE-trending faults and a prevalent normal component along the WSW–ENE- trending faults (Pirrotta et al., 2021). The activity of this fault system is evidenced by the multiple river deflections in the drainage network (Pirrotta et al., 2022).

3. Material and methods

High-resolution multibeam bathymetry and seismic reflection profiles were acquired in several surveys during the oceanographic cruises listed in Table 1.

3.1. High-resolution multibeam bathymetry, backscatter data and ROV videos

Multibeam bathymetry data were collected by means of four echosounder systems in different oceanographic cruises (Table 1). The Teledyne Reson SeaBat 7111 (100 kHz) and 7160–8160 (44–50 kHz) systems were used to map the deepest seafloor (from 800 to 2000 m wd), while the Kongsberg EM710 (70–100 kHz) and EM3002D (300 kHz) to investigate shallow-water seafloor (from about 10 m to 1000 m depth). During the bathymetric surveys, a patch test of multibeam transducers on specific target was performed in areas close to the survey zone, preceded by sound velocity profiles. All multibeam datasets were processed using the Caris Hips & Sips (8.1–13.1) hydrographic software and specific procedures (Bosman et al., 2015; Bosman et al., 2020). Multibeam data processing included: 1) patch test of transducers, 2) sound velocity analysis and raytracing of the acoustic signals, 3) tide corrections using time-series data recorded from the National tide gauge network (https://www.mareografico.it/), 4) statistical and geometrical filters to remove coherent and incoherent noise, 5) statistical and manual filtering of spikes. Soundings data were gridded, generating high-resolution Digital Elevation Models (DEMs) with cell sizes varying from 0.5 to 2 m in shallow water (<100 m) to 10 m in intermediate water (100–500 m) and 15–20 m in deep water (>500 m). Multibeam intensity backscatter data were processed only for Kongsberg EM710

Table 1

Multibeam, seismic and side scan sonar surveys carried out in the SEG during oceanographic cruises and details of the equipments used in the geophysical survey. Multibeam echosounder (MBES), Multibeam Backscatter Intensity (BSI), Side Scan Sonar (SSS), Research Vessel (R/V).

Survey	Year	MBES	MBES BSI	Chirp kHz	Sparker kJ	Uniboom kJ	SSS kHz	Positioning	R/V
Calabria 85	1985	–	–	–	–	0.3	–	Loran C	Urania
Iddusics	2004	Teledyne 8160	–	Datasonic 2–7	–	–	–	DGPS	Universitatis
Kalet	2007	Teledyne 8160	–	Datasonic 2–7	G&G - 4	–	–	DGPS	Urania
Magic IGAG	2010	Teledyne 7111	Yes	–	–	–	–	DGPS	Maria Grazia
Magic IGAG	2010	Teledyne 7160	Yes	GeoAcoustic	–	–	–	DGPS	Minerva 1
Magic IGAG	2011	EM710	Yes	Datasonic	GeoRes.- 2	–	–	DGPS	Urania
Magic IGAG	2012	EM710	Yes	Datasonic	–	–	–	DGPS HP	Urania
TyGraF	2013	EM710	Yes	Datasonic	GeoRes.- 1.5	–	Edgetech	DGPS HP	Urania
EPAF	2019	–	–	–	GeoSource-DS	–	–	DGPS	Atlante

echosounder, generating a backscatter map. All cartographic maps were projected in UTM 33 N, Datum WGS84. Side scan sonar data were also acquired along the F1 fault. These data were processed using slant range corrections, time-varied gain (TVG) and algorithms to automatic normalisation (AGC) and de-striping. One ROV video transect was performed along the fault F1 escarpment in the 2012 survey. The video images were collected using the GEI-Pollux III system equipped with a digital camera (Sony CCD 1/3″) and a high-definition camera (SonyHDR-HC7) positioned with differential GNSS system from the vessel.

3.2. High-resolution seismic reflection profiles

High-resolution seismic reflection profiles (Fig. 1b) were collected during several cruises by CNR-IGAG, onboard R/V Urania (in 1985, 2006, 2011 and 2012), R/V Universitatis (2004) and R/V Minerva1 (2010). Seismic data were acquired using the Chirp II (Datasonic) sub-bottom profiler, multi-tips Sparker (1–4 kJ) and Uniboom (0.3 kJ) sources. The 2–7 kHz, sweep-modulated bandwidth Chirp source was used to collect high resolution seismic data. The chirp operates with 16 transducers in a wide frequency band (2–7 kHz), and a chirp pulse of 20–30 ms. Data were recorded with a 0.8 s sweep in deep water and a 0.25 s sweep in shallow water. Data processing included the following mathematical operators: a) true amplitude recovery using a T^2 spherical divergence correction, and b) time-variant gain to boost amplitudes of deeper arrivals. Signal penetration exceeded 90 ms two-way time (t.w.t.) in the deeper sector of the slope. Vertical resolution is up to 20–50 cm. The Sparker data were acquired using a one to four kJoule Geo-Source Sparker acoustic source with a multi-tip Sparker array and a single-channel streamer with an active section of 2.8 m. The shooting interval was 1.5 s with a 1.2 s record length and 0.1 ms sampling interval. Data processing included the following mathematical operators: true amplitude recovery using a T^2 spherical divergence correction; band-pass (200–2000 Hz) "finite impulse response" filter using a filter length of 256 samples; swell-filter; deconvolution; multiple attenuations; trace mixing of three traces for enhancing horizontal signal; time-variant gain to boost amplitudes of deeper arrivals; mutes to eliminate the signal noise on the water column. We found that signal penetration exceeded 200 ms t.w.t. The vertical resolution was up to 0.8 m in the near sub-seafloor. Additional analogue Uniboom seismic profiles with intermediate resolution and penetration were used for this study. Data were filtered using a 400–4000 Hz band-pass filter and relied on an EPC graphic recorder with a 0.25 s sweep. Uniboom profiles were converted from raster to SEG-Y format, georeferenced and included in the digital dataset.

The reference system for all geophysical data is the WGS84 with a UTM 33N projection. The whole seismic dataset was merged with the high-resolution DEMs to allow integrated interpretation. The sediment thickness and depths were derived from the time to depth conversion, using velocities of 1515 m/s and 1650 m/s for the water column, post- and pre-Last Glacial Maximum (LGM) deposits, respectively. We derived these values from sound velocity profiles and sonic log data acquired in

coeval deposits with similar offshore settings (Ferranti et al., 2019).

3.3. Active fault mapping by seismic reflection profiles and multibeam data

Active faults were identified from lateral offsets of the upper part of Quaternary deposits in high-resolution seismic reflection profiles and linear seafloor scarps on multibeam data. Moreover, they were identified by detecting hyperbolic diffractions and/or progressive tilting of adjacent reflectors. The recognition of fault scarps on multibeam bathymetry allowed the accurate correlation between fault segments through seismic profiles. The integration of multibeam bathymetry and seismic profiles allowed the measurement of fault orientation, plunging, vertical displacement (fault throws) and fault activity. Fault throws were measured on seismic profiles as differences in t.w.t. between footwall and hanging wall cutoffs, subsequently transformed in distances. Seafloor displacements were measured on main faults using seafloor throws measured on multibeam bathymetry.

Chronological constraints for the tectonic deformations were derived by interpreting the subaerial erosional surface formed during the LGM at 18–23 ka BP (Yokoyama et al., 2000) and the maximum flooding surface. The first surface formed when the sea level was ~120–130 m below its current position (Lambeck et al., 2011), whereas the maximum flooding surface (MFS), which should have an age of about 6 ka BP (Ruello et al., 2017), is a downlap surface that separates the transgressive and highstand deposits. Both these horizons were interpreted using sequence stratigraphy concepts developed for high-order Pleistocene sequences (e.g., Posamentier et al., 1992; Hernandez-Molina et al., 2000; Lericolais et al., 2001) and by correlation with seismo-stratigraphic models provided in previous studies carried out in the study area (Chiocci et al., 1989; Trincardi et al., 2003; Martorelli et al., 2010a; Corradino et al., 2021).

4. Results

The interpretation of high-resolution multibeam bathymetry and seismic profiles reveals a complex pattern of seabed morphologies and deposits deeply affected by fault activity, both on the shelf and slope sectors of the SEG (Fig. 2a). Morphological features related to fault activity or affected by tectonics identified on multibeam bathymetry (e.g., canyon and channels, linear escarpments and pockmarks) are described in Section 4.1. Section 4.2 describes the seismo-stratigraphic characteristics of key horizons displaced by faults (e.g., the LGM-U and MFS) and of Late Quaternary deposits. Section 4.3 describes the systems of active faults and shows the main characteristics of fault deformation (e.g., throws and across-fault thickness changes) derived by seismics and multibeam bathymetry.

4.1. Seafloor morphology

The investigated area of the SEG includes the continental shelf and the upper sector of the continental slope, separated by a shelf break
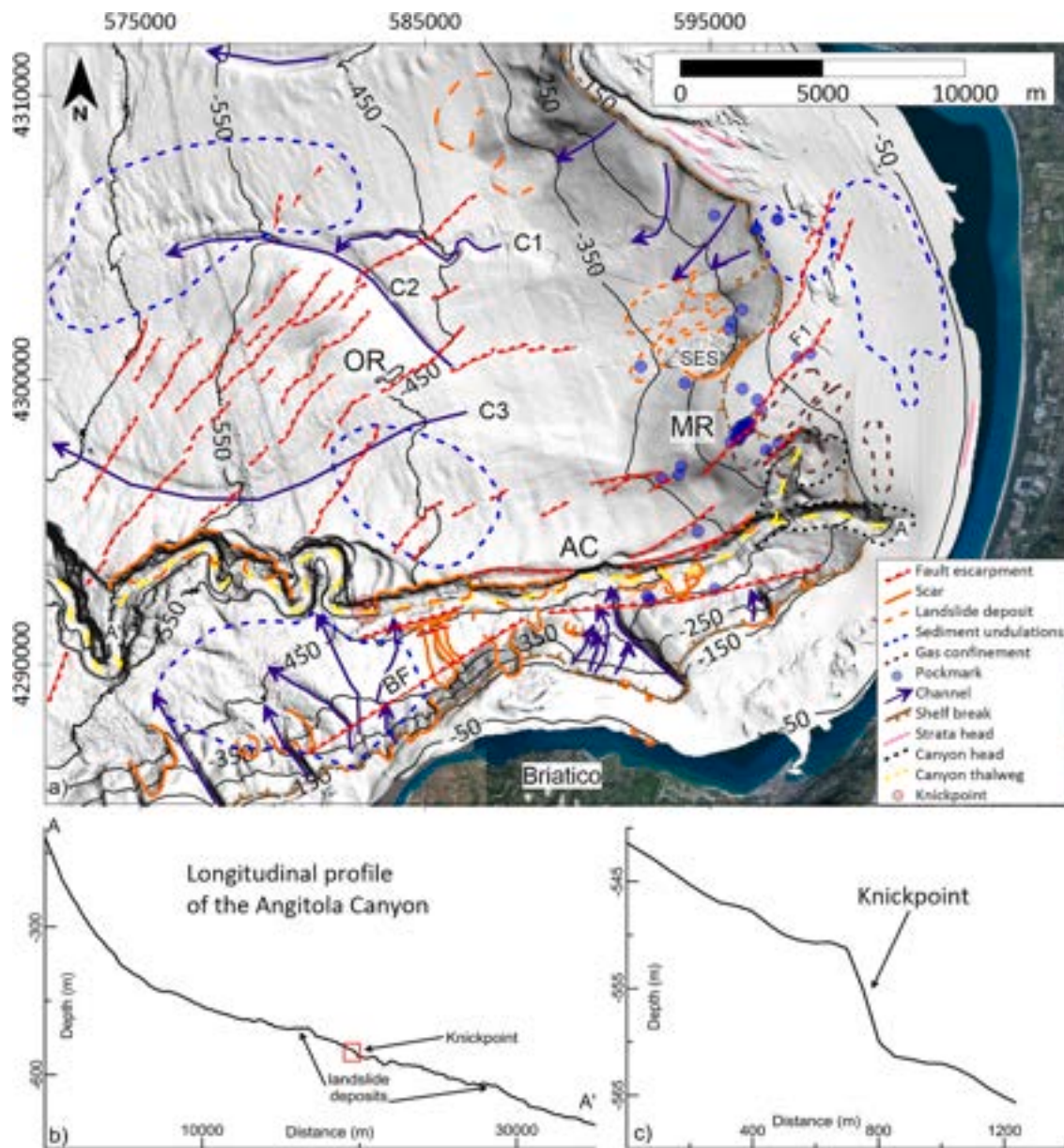
Fig. 2. a) Morphostructural map of the S. Eufemia Gulf with indication of the main seabed morphological and tectonic features. SEE: S. Eufemia Fault Escarpment; SES: S. Eufemia Slide; BR: Briatico Fault Escarpment; MR: Maida Ridge; O: Offshore mounded Relief; AC: Angitola Canyon. C1-C3: turbidite slope channels. b) Longitudinal depth profile of the Angitola Canyon (see A–A′ in a for location). c) Detail of the depth profile showing a knickpoint.

located between 140 and 160 m water depth (wd; Fig. 2a). The continental shelf is <1 to 9 km wide and has slope gradients between 0.5° (in the central sector) and >1° (in the southern sector, off Briatico, Fig. 2a). On the continental shelf, the main morphological elements are a NE-SW oriented ridge (the Maida Ridge, MR in Fig. 2a), crossed by a set of NE-SW fault escarpments, and the head of the Angitola Canyon. The upper sector of the continental slope has a mean gradient of 3–4° and is characterised by several erosive features (channels, canyons, slide scars) and faults escarpments. In this sector, the main morphological element is the upper reach of the Angitola Canyon that runs E-W along the southern SEG. This canyon separates two distinct areas of the continental slope: 1) gentle seafloor gradients (<2°) characterise the northern area that is dominated by a mounded morphology (the offshore mounded relief, OR in Fig. 2a) and by an array of fault escarpments, mostly oriented NE-SW; 2) steeper seafloor gradients (locally up to 12°) characterise the southern area, where a NE-SW oriented fault escarpment in the uppermost sector of the continental slope and diffuse mass-wasting features are

present.

4.1.1. The Angitola Canyon

The Angitola Canyon starts at about 85 m water depth (afterwards wd) and indents the outer shelf (Fig. 2a). Within the SEG, it is 1–2 km wide and 200–800 m deep. It can be subdivided in three segments: 1) the canyon head; 2) a straight segment oriented ENE-WSW; 3) a meandering segment oriented E-W. The canyon head is composed of two branches (Fig. 2a). The northern branch is 1.8 km wide and roughly oriented NE-SW, indenting the continental shelf for 1.8 km; the northern edge of this branch has a linear trend, sub-parallel to a fault escarpment. The southern branch is 1.3 km wide, roughly oriented E-W and indents the continental shelf for 2.2 km, reaching a distance of 2.5 km from the shoreline. The straight segment begins at 380 m wd and is 18 km long. The meandering segment starts at 550 m wd and develops adjacent to the area characterised by the NE-SW linear escarpments. This segment is composed of a complex pattern of meanders that alternates with straight

sectors. Along the thalweg a knickpoint occurs at around 550 m wd, characterised by a 10 m high and 7° steep scarp (Fig. 2b and c).

4.1.2. Fault escarpments

Faults escarpments are widespread in the study area, forming an array of sub-parallel linear features (Fig. 2a), mainly oriented NE-SW in the deeper area of the continental slope and on the continental shelf, and ENE-WSW in the area close to the straight segment of the Angitola Canyon. Almost all the observed linear escarpments are fault scarps affecting the seabed (Corradino et al., 2021); see Section 4.3 for further details. Furthermore, a main NE-SW oriented fault escarpment (dipping toward NW; BF in Fig. 2a), 15 km long and 450 m high, is recognisable south of Angitola Canyon. Only in a few cases (e.g., the NW-SE oriented escarpments located off Capo Suvero) the linear escarpments may represent strata heads (Fig. 2a) generated by differential erosion and encrusted by organisms.

4.1.3. Landslides

Several slide scars and deposits occur in the SEG, typically affecting the shelf break-upper slope sector and the flanks of the Angitola Canyon (Fig. 2a). Major slide deposits occur in the northern area, between 350 and 450 m wd, at the slope break that divides the high gradient (4°) sector of the upper continental slope from the low (2°) gradient one. Slide deposits have a surface of 2.5–4 km² and a relief of 5–8 m. Chaotic morphologies and rafted blocks are frequent within slide deposits. The main slide (SES in Fig. 2a) is located on the northern flank of the Maida Ridge, affecting the seafloor adjacent to the shelf break. Its scar is 2.4 km

wide, 440 m long and 10 m deep. The slide deposit occurs at the toe of the Maida Ridge, covering an area of 2.8 km², with rafted blocks and pressure ridges. The slide scar and deposits of the S. Eufemia slide have a "fresh" morphological appearance which differs from all other deposits identified in the SEG. Several small (0.5–1.5 km wide on average) coalescent slides occur along the flanks of the Angitola Canyon with blocky deposits accumulated in the Canyon thalweg. Further slides are present along the Briatico escarpment.

4.1.4. Sediment undulations

On the continental shelf off the Amato river, smooth and relatively regular sediment undulations, mostly oriented at a right angle with respect to the mean seafloor dip are present between 50 and 140 m wd (Figs. 2a and 3a), covering a surface of about 22 km². They have wavelengths of 40–120 m and heights <1–1.5 m. They are often asymmetric in cross-section, with downslope flanks steeper than upslope flanks, developing on slope gradients of about 0.5–3°. Their morphology, alignment (crest oriented parallel to the isobaths) and subsurface seismic characteristics (Fig. 3b; e.g., development of basal surfaces along different stratigraphic levels, lack of continuity of reflections between undulations and local chaotic facies; see Section 4.2.1 for further details) suggests that the majority of the observed sediment undulations can be interpreted as creep deformation (e.g., Shillington et al., 2012). Alternatively, they may be interpreted as depositional cyclic steps formed by turbidite flows (Slootman and Cartigny, 2020).

On the continental slope, trains of concentric bedforms with downslope-convex crest lines in plan-view are observed off Briatico
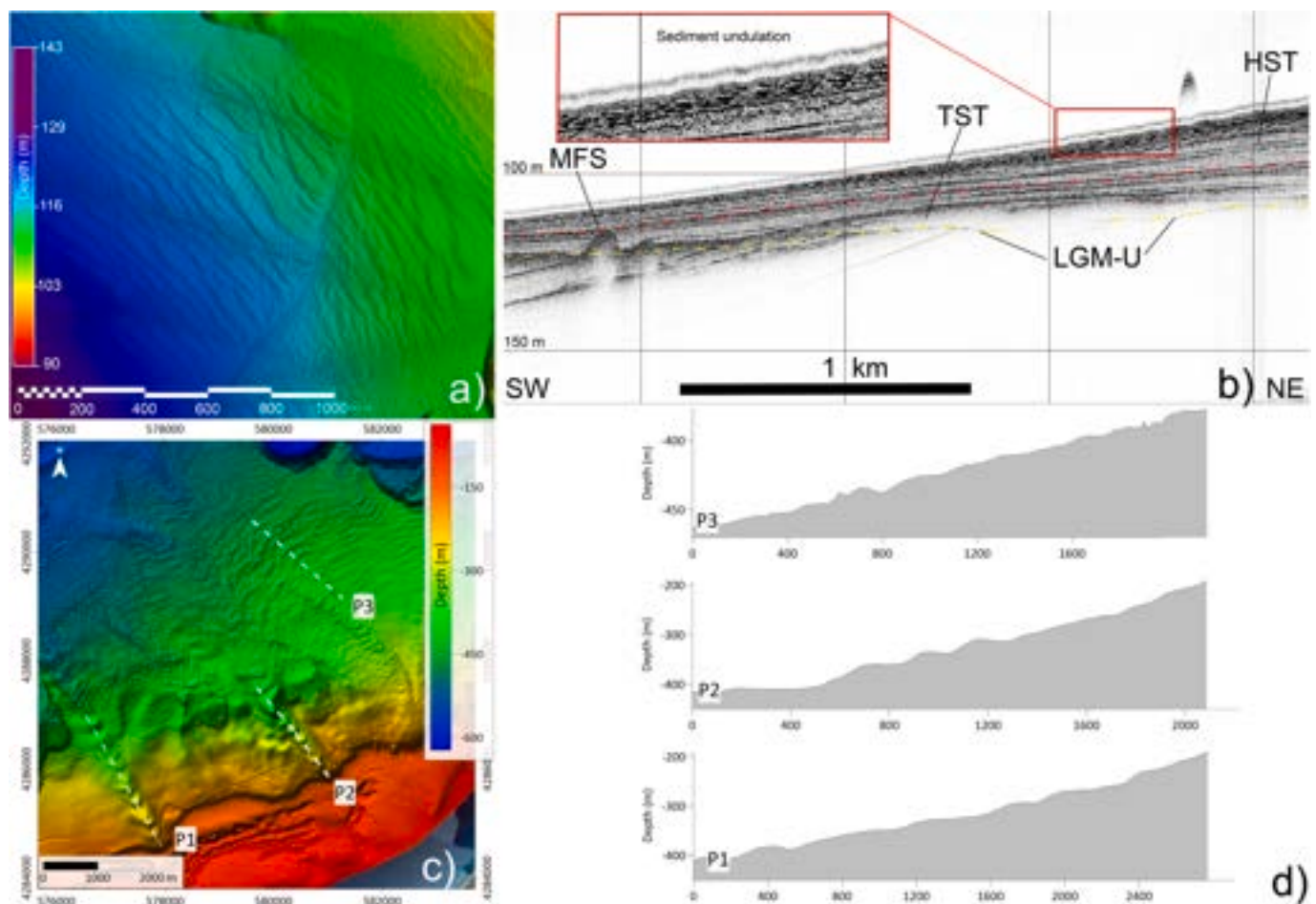

Fig. 3. a) High resolution multibeam bathymetry showing sediment undulations on the continental shelf. b) Chirp seismic profile HR1 showing sediment undulations affecting the seafloor and the upper part of highstand deposits; the size of sediment undulations decreases downslope as the slope gradient decrease. c) Multibeam bathymetry showing upper-flow regime bedforms. d) Bathymetric profiles across crescent-shaped bedforms (P1 and P2) and concentric bedforms (P3).

(Fig. 3c and d). They are mostly oriented at a right angle with respect to the mean seafloor dip, developing on slopes of 2.3–3°, and fade out downslope at a gradient of about 1°. They have wavelengths of 100–250 m, heights of 2–12 m, and are often asymmetric in cross-section, with downslope flanks steeper than upslope flanks. These concentric bedforms form a field that covers a surface of about 23 km² located on the continental slope, between 300 and 520 m wd; further fields of similar concentric bedforms are present north of the Angitola Canyon and the slope channel C2 (Fig. 2a). Moreover, off Briatico, coaxial trains of bedforms with arcuate or crescent-shaped crest lines in plan view are present within slope channels cutting the field of downslope-convex bedforms (Fig. 3c). These crescent-shaped bedforms have a wavelength of 130–350 m, a height of 4–25 m, and are asymmetric (with downslope flanks steeper than upslope flanks), developing on slope gradients of 2–5°. Based on their size, morphology and seismic characteristics indicating an upslope migration, both these bedforms are interpreted as upper-flow regime bedforms related to turbidite flows (e. g., Kostic, 2014; Slootman and Cartigny, 2020; Postma et al., 2020). This is also suggested by their association with fan-shaped deposits resembling turbidite slope fans, similar to those described in nearby areas (Casalbore et al., 2014; Martorelli et al., 2022). More in detail, the crescent-shape concave bedforms could be interpreted as the result of net-erosional cyclic steps, whereas the interpretation of the convex-shaped bedforms could be related to net-depositional cyclic steps (e.g., Slootman and Cartigny, 2020 and reference therein); this last interpretation is also supported by the positive position of the crests relatively to the surrounding region of the seafloor, suggesting a general deposition from turbidity currents in this area.

4.1.5. Pockmarks

Sub-circular and V-shaped depressions, 20–40 m wide and a few meters deep are distributed on the outer continental shelf-upper slope sector, between 110 and 300 m wd. Based on their morphology, these depressions are interpreted as pockmarks (sensu Hovland and Judd, 1988). They occur either as isolated features or are distributed along the direction of linear escarpments. The most important alignment is present along the S. Eufemia fault escarpment, between 160 and 200 m wd.

Here, tens of pockmarks are distributed along a 2 km long and 300 m wide NE-SW belt (Fig. 4). Another field of pockmarks is present along the northern branch of the Angitola Canyon head (Fig. 2a). They are some tens of meters wide and distributed along the NE-SW direction.

4.2. Seismic stratigraphy

4.2.1. The Late Quaternary depositional sequence

On the shelf, the LQDS is composed of a wedge-shaped seismic unit that pinches out toward the shelf-break, bounded at its base by a regional erosional surface associated with the LGM unconformity (LGM-U, yellow line in Fig. 5). This unconformity is a seaward dipping surface, that is detectable throughout the continental shelf area, because of its high-amplitude reflection and angular discordance. Below a depth of about 135–175 m, the LGM-U becomes a correlative conformity (Fig. 5a). The wedge-shaped seismic unit is present throughout the continental shelf with a notable thickness, reaching up to >70 ms t.w.t. (about 56 m) off the Amato river (Martorelli et al., 2010a). In distal areas, it typically thins to 10–12 ms t.w.t. (about 8–9.6 m), blanketing the seafloor. It consists of two seismic sub-units, separated by the maximum flooding surface (MFS), which is a high amplitudes-high continuity, downlap surface on dip seismic profiles (Fig. 5a) that can be traced in almost all the shelf. The lower sub-unit is composed of prograding parasequences arranged in a retrogradational stacking pattern associated with the transgressive systems tract (TST). The upper sub-unit comprises progradational or aggradational parasequences associated with the highstand systems tract (HST). The TST is composed of 2–3 parasequences characterised by high-amplitude prograding reflections (Fig. 5a). The TST deposits form isolated depocentres controlled by the local topography of the basal surface (Martorelli et al., 2010a). The main depocentre is 40 ms t.w.t. (about 32 m) thick and is located off the Amato River; whereas the TST deposits are nearly absent on the Maida Ridge (Fig. 5c). The HST is relatively continuous over the shelf, attaining a maximum thickness of 30 ms t.w.t. (about 24 m) offshore of the Amato River (Martorelli et al., 2010a). The external geometry of the HST is wedge-like on the inner shelf and almost tabular on the outer shelf (Fig. 5a). Its thickness diminishes rapidly seaward to a
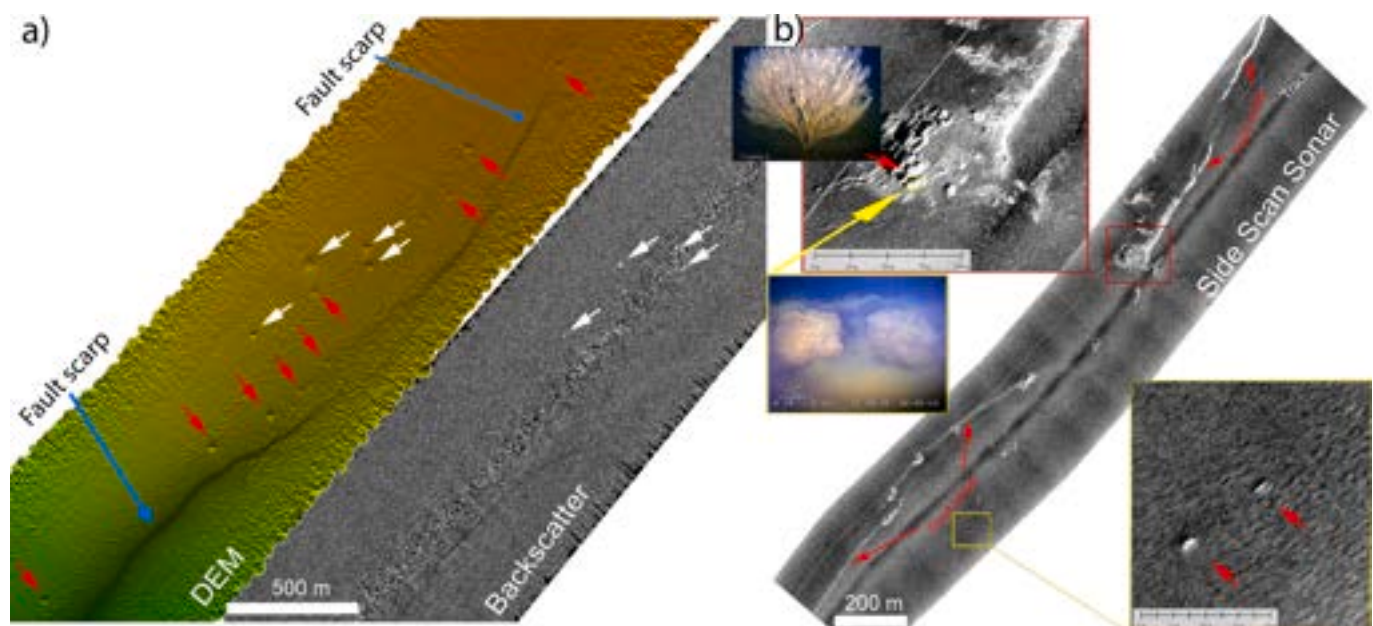

Fig. 4. a) Comparison between high-resolution multibeam bathymetry and backscatter data of the main pockmark field located along the Fault F1scarp. The backscatter data show four pockmarks (white arrows) characterised by high backscatter intensity along the fault. b) Very high-resolution side scan sonar image of the Fault F1showing small pockmarks along the fault and isolated outcrops (see ROV image in the yellow box) several meter high and tens of meters wide surrounded by coarse sediment (see high backscatter intensity), possibly due to biogenic debris. See Fig. 1c for location. (For interpretation of the references to color in this figure legend, the reader is referred to the web version of this article.)
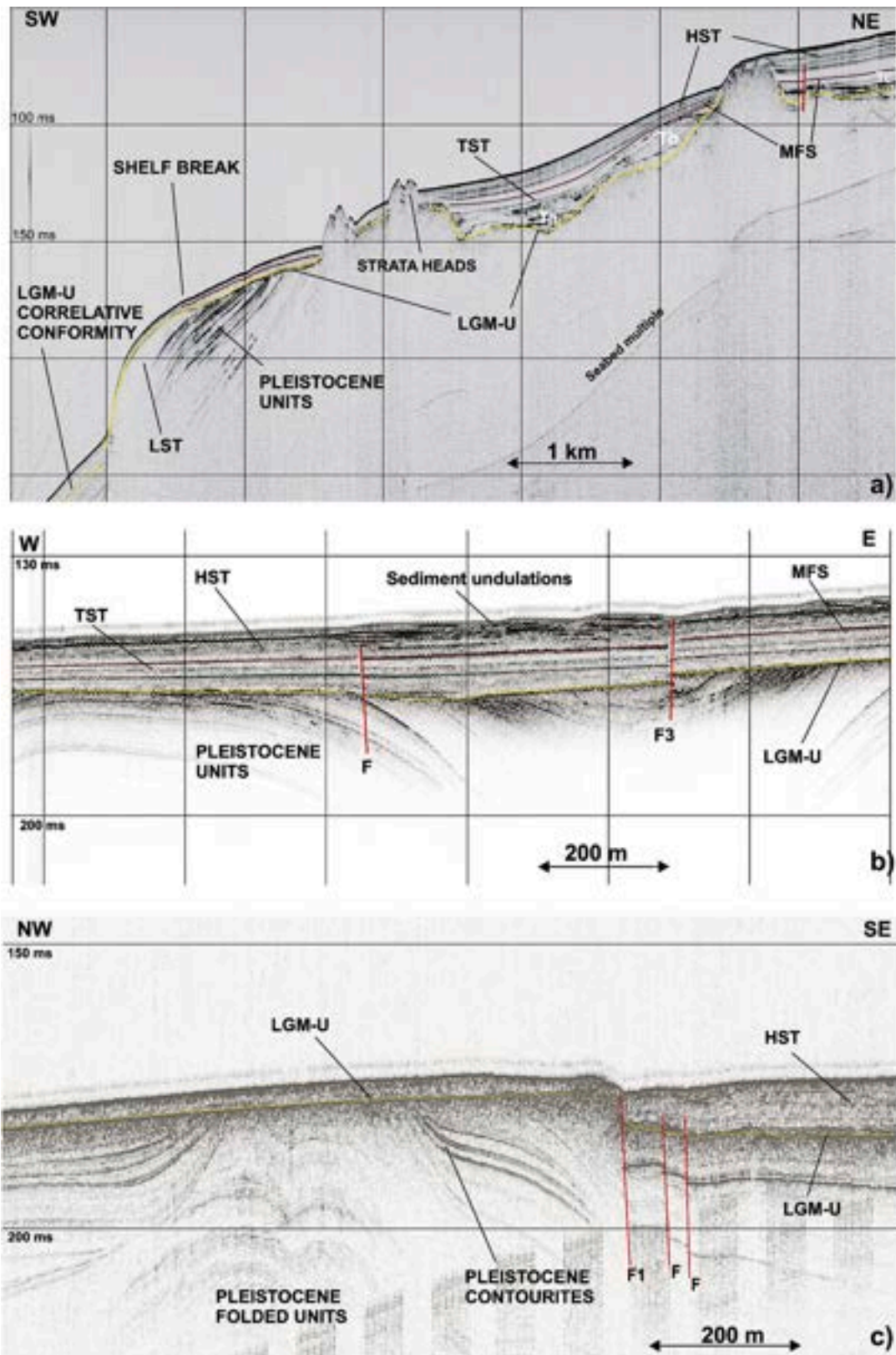
Fig. 5. a) Dip Sparker seismic profile ST24 across the Late-Quaternary Depositional Sequence (LQDS) resting above the Last Glacial Maximum unconformity (yellow horizon). Violet horizon: the maximum flooding surface separating transgressive (TST) and highstand (HST) deposits. The southwestern sector of the profile shows the wedge-shaped prograding deposit (LST) formed during the LGM. b) Strike Chirp seismic profile SE15 across the LQDS showing sediment undulations affecting the seafloor and the upper part of highstand deposits; on the right side fault F3. c) Chirp profile FS Eufemia_26 across fault F1 and the Maida Ridge; paleocontourite deposits are present on the flank of the Maida Ridge. See Fig. 1b for location. (For interpretation of the references to color in this figure legend, the reader is referred to the web version of this article.)

constant value of 2–5 ms t.w.t. (1.6–4 m). The HST is absent or thinner than 1 ms t.w.t. (<0.8 m) on the morphological highs. It consists of 2 parasequences characterised by different seismic facies. The lower parasequence lies directly on the MFS and shows a semi-transparent seismic facies throughout the shelf (Fig. 5a). High continuity-high amplitude reflections typically characterise the upper parasequence. In the central-eastern shelf sector, an undulating internal configuration of seismic reflectors (Figs. 3b and 5b) is frequently observed, which is detectable also in the seabed morphology (Fig. 3a). This configuration has a max thickness of 8–10 ms t.w.t. and is rooted on different subsurface horizons (Fig. 3b). Tilting of subsurface reflectors is frequently observed and locally, the thickness of undulated sediment increases as the slope gradient increases (e.g., on the hangingwall of fault F4). Moreover, a direct relationship between the size of undulations (wavelength and height) and the slope gradient is locally observed (e.g., at the hanging-wall of fault F2). Main sectors characterised by this undulated configuration are located nearby the main faults (e.g., on the hanging wall of fault F2, in the sector comprised between the tip of faults F1 and F2) and close to the Amato River depocentre of LQDS deposits where gas-charged sediment is present landward. As indicated in Section 4.1, these undulations may represent creep deformation or depositional cyclic steps.

Along the shelf break, the LQDS includes a wedge-shaped prograding unit that can be observed both in the northern and southern sectors of the SEG. This prograding unit has been associated with lowstand deposits (LST in Fig. 5a) formed below the wave-base level (Chiocci and Orlando, 1996; Pepe et al., 2014). It is 20–30 ms t.w.t. thick and elongated along the shelf break, with a depositional edge located between 170 and 135 wd. In the northern sector, the LST fills paleo-channels, whereas in the southern sector it is interrupted by slide scars or canyon-channel heads.

Beyond the shelf break, the LQDS is typically composed of acoustically-transparent drape deposits resting above the LGM correlative conformity (Fig. 5a). Typically, these drape deposits are a few meters thick in the basin sector (Trincardi et al., 1995).

4.2.2. Pre-Late Quaternary deposits

On the shelf sector, pre-Late Quaternary deposits are characterised by oblique progradational seismic units located below the LQDS (Fig. 5a). These units are related to Plio-Pleistocene slope deposits (Chiocci and Orlando, 1995). On the slope sector, they are typically represented by aggrading units characterised by high amplitude-high continuity reflections, interpreted as turbidites (Trincardi et al., 1995). On the NW flank of the Maida Ridge, buried mounded deposits resembling contourite drifts (e.g., Rebesco et al., 2014) are present (Fig. 5c). Moreover, landslide deposits embedded within pre-Late Quaternary deposits are observed at the base of the upper slope off Capo Suvero, in a paleo-topographic low confined by the offshore mounded relief.

4.3. Faults systems

Based on the high-resolution multibeam bathymetry and seismic profiles several high-angle faults have been mapped (Fig. 6a) and characterised in their geometry and deformation (Fig. 6b). They form an array of sub-parallel lineaments and some fault traces appear as arrays of minor en-echelon segments (e.g., F14 and southern prolongation of fault F1 in Fig. 6a). Faults are normal, a few hundred meters to 9–10 km long, and spaced from a few hundred meters to 2–3 km. Most faults offset LQDS deposits and reach the seafloor, with vertical displacements varying from <1 m up to 12 m. The vertical slip varies along the strike of each fault (Fig. ES1), with a maximum value toward their centre or, in some cases, toward their tip. The vertical displacement of the LGM unconformity is higher than 3.2 m and 8 m in about 60 % and 20 % of the faults, respectively. About 30 % of the faults have a length >5 km. The plot of maximum throw vs length indicates a positive correlation between throw values and fault lengths (Fig. 6b).

Based on the fault planes' distribution and strike direction (Fig. 6a), these faults can be grouped into: 1) the S. Eufemia fault system, with fault planes mainly oriented from N26E to N40E, on the continental shelf off S. Eufemia village; 2) the offshore fault system, characterised by fault planes mainly oriented from N28E to N60E, on the continental slope off Capo Suvero; 3) the Angitola Canyon fault system, with fault planes oriented from N60E to N85E, located in the area adjacent to the canyon. Although almost all of the mapped faults offset the seabed, a subordinate set of buried or blind faults (e.g., F2, F4, F5, F6, F9 and F10) are identified in all fault systems.

4.3.1. The S. Eufemia fault system

The S. Eufemia fault system includes faults F1, F2, F3, F4 and FA (Fig. 6a). Faults F1 and F2 dip toward SE, whereas F3 and F4 dip toward NW. They offset Late-Quaternary deposits on the continental shelf-upper slope reaching the seafloor and form an array of sub-parallel linear escarpments between 35 and 300 m wd. Fault F1 is characterised by the highest fault length (about 9.5 km) and its escarpment locally shows 2–3 slope breaks, producing 0.5–1 m high steps (Fig. 2a). Sub-parallel to the F1 escarpment, other minor scarps (1–2 km long, 1 m high) are present around the tip region. The LQDS faulted deposits thicken >100 % across the fault and the fault confines gas in the hanging wall side, as indicated by acoustic turbidity and bright spots (Fig. 10a and b). In its central part, at least two rupture events can be recognised. Three steps record a max LGM throw of 5.5 m. In detail, two segments can be defined (Fig. 7a) based on the variability of the offset along the fault strike: 1) the segment CN, which includes the central and northern part of the fault F1 (yellow line in Fig. 7a), is characterised by subsurface displacement that reaches the seafloor in its central part (Figs. 5c and 7d); 2) the segment ST, which corresponds to the southern part of the fault F1 (red line in Fig. 7a), is characterised by a deep rupture (50 m below the seabed) beneath folded strata. Along the CN segment, seafloor throw varies between 0.8 and 4 m (see orange line in Fig. 7b). In the northern part of the CN, the fault F1 offsets the TST deposits, part of HST deposits and older Pleistocene prograding units. Here, the rupture is a few meters below the seafloor (Figs. 8 and 9) and the displacement increases downwards, from 0.8 m (MFS throw) to 2.4 m (LGM-U throw, grey line in Fig. 7b). The long-term vertical slip rate computed on the LGM erosional surface interpreted in the seismic Line ST5 is 0.24 mm/yr. Along the segment ST (red line in Fig. 7a), the fault F1 cuts the lower part of the Pleistocene units and older deposits, whereas the upper part of Pleistocene units and the recent deposits are folded (red line in Figs. 7a, 10b).

Fault F2 (Fig. 6a) is a SE-dipping tectonic lineament characterised by high throw and length values. It develops on the shelf between 35 and 100 m water depth. This fault offsets the LGM-U and MFS surfaces with a throw up to 5.6 and 1.6 m, respectively, but does not reach the seafloor (Fig. 9). Fault FA dips toward SE and bounds the northern head of the canyon (Figs. 6a and 10). Faults F3 and F4 dip toward NW and develop west to the northern sector of fault F1 (Figs. 6a and 9). F3 offsets the LGM-U reflector by about 3.2 m, whereas the throw measured at the seafloor is about 2.4 m. The F4 throw measured at the LGM-U reflector and seafloor is about 80 cm.

4.3.2. The Angitola Canyon fault system

This system includes faults F5, F6, F10, F11 and F12 that confine the straight segment of the Angitola Canyon, between about 350 and 450 m wd (Figs. 6a and 10c). They are ENE-WSW oriented, dipping toward north and the south, 1.2–9.6 km long and show small throws or extensional drag folds. Faults F5 and F6 dip toward the south, whereas faults F11 and F12 toward the north. The lateral offset of reflectors across faults F5 and F6 are not recognisable but folded strata within LQDS deposits and the upper part of Pleistocene units (Fig. 10c) are observed. They show a normal-drag geometry that is consistent with fault propagation folding.
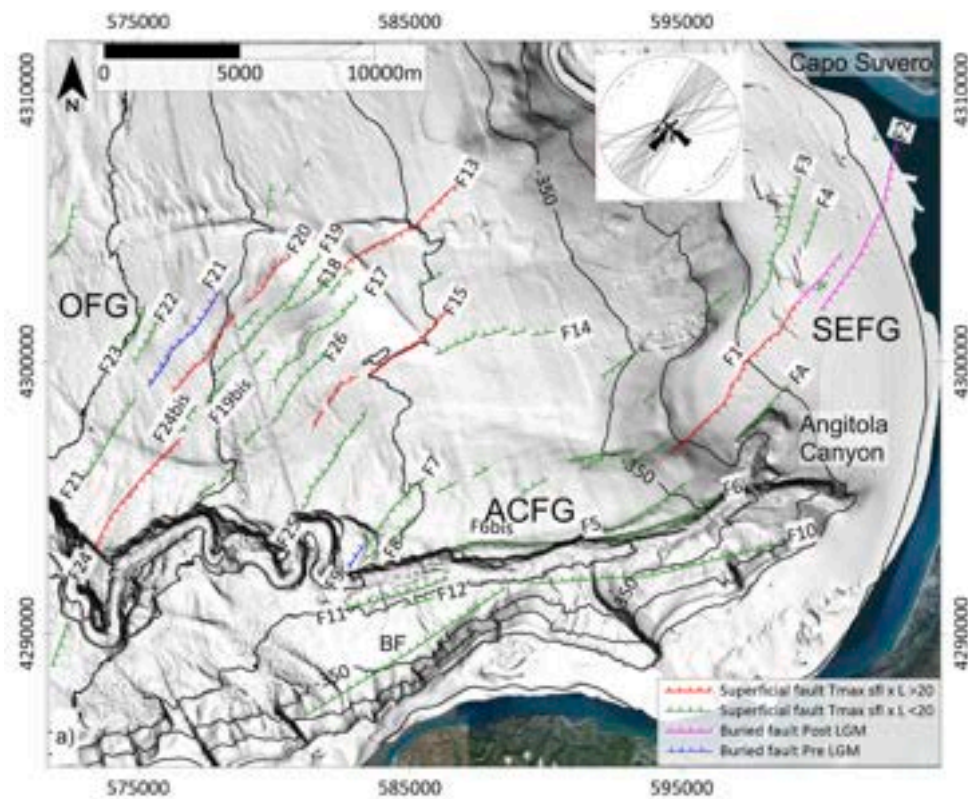
Fig. 6. a) Fault map showing: main normal faults (the triangles indicate the downthrown side-hangingwall) deforming the seafloor (red; Tmax sfl × L > 20; green Tmax sfl × L < 20); buried faults deforming postglacial deposits (pink), buried faults deforming only pre-LGM deposits (blue), faults with only surficial throw (black). Faults labeled in red have the same throw for the seafloor and the LGM/Holocene. Fault F1 coincides with the central part of the S. Eufemia fault (SEF in Fig. 1a) identified by Loreto et al. (2017). The inset shows the orientation of poles to fault planes. b) Max throw (ms t.w.t.) vs length (m) for seafloor (black diamonds) and-LGM-U (red circles) displacement. (For interpretation of the references to color in this figure legend, the reader is referred to the web version of this article.)
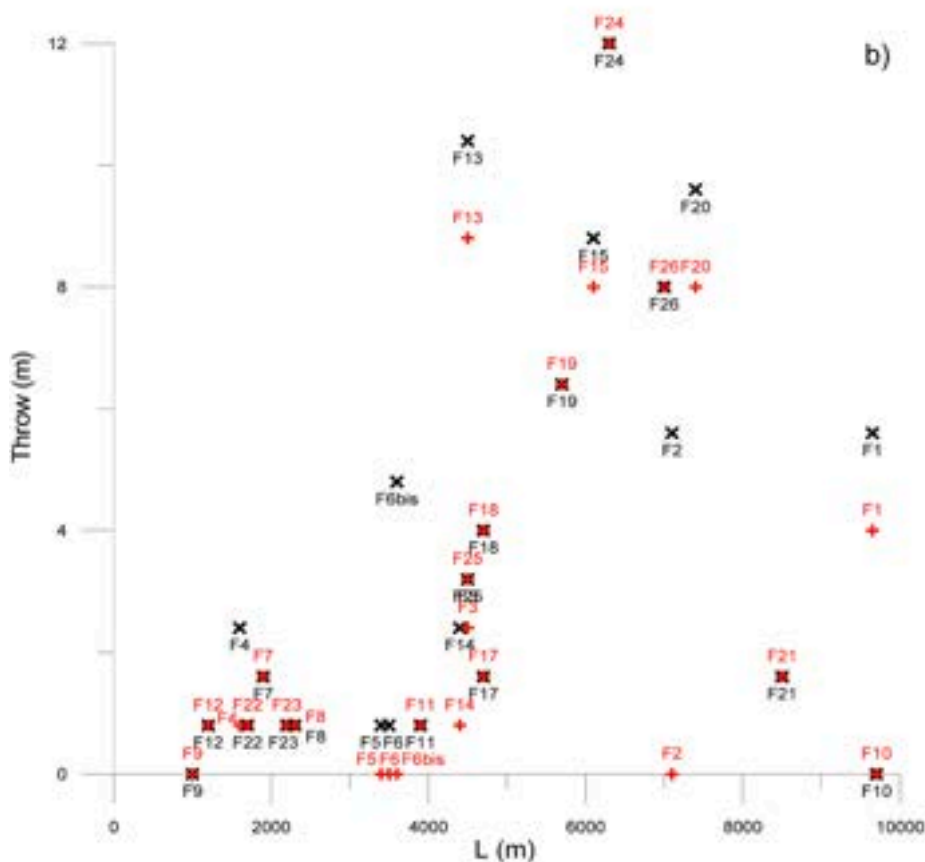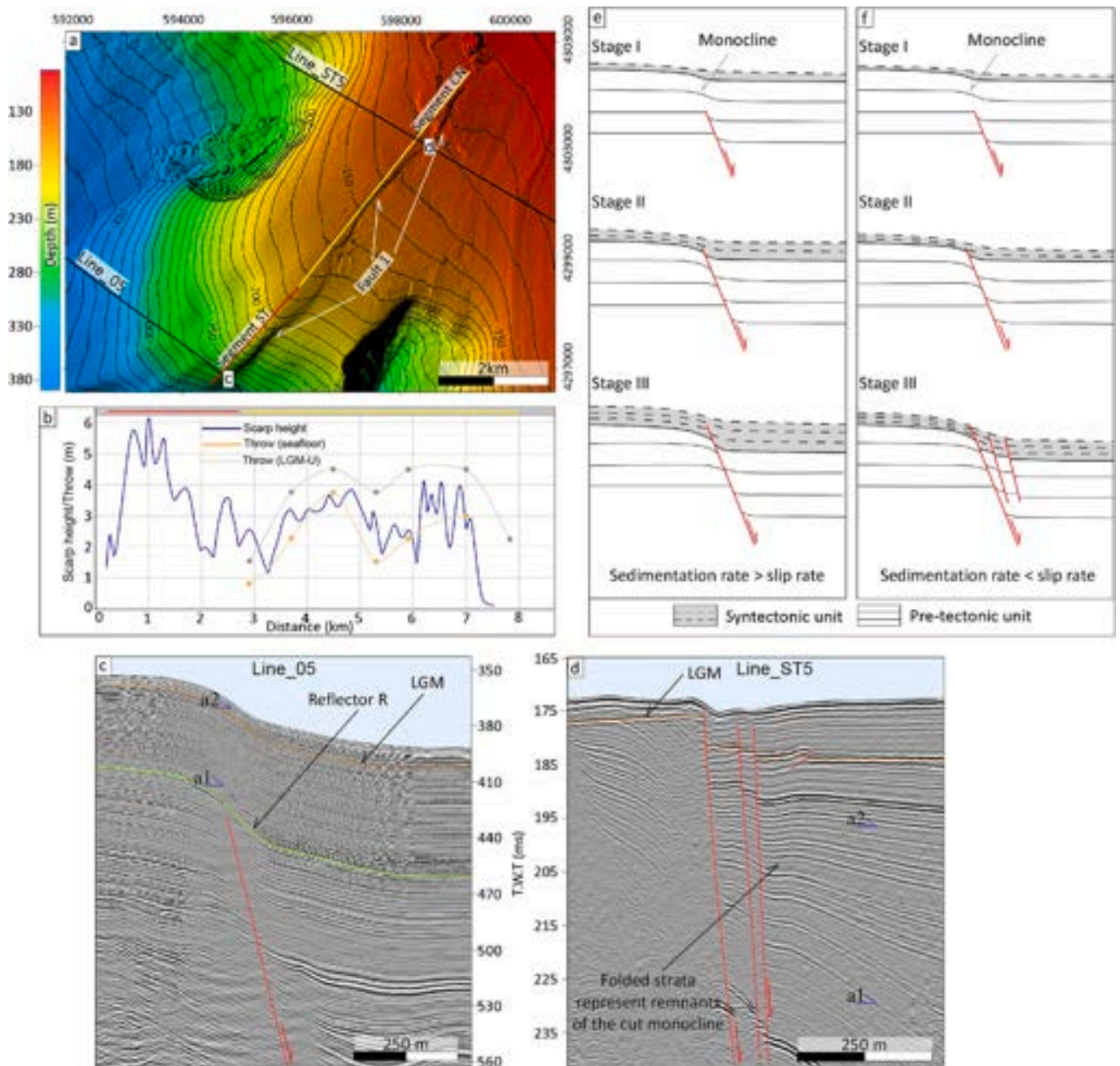
Fig. 7. a) Detail of the F1 fault and its two segments (CN and ST) with different scarp height/throw inferred from high-resolution multibeam bathymetry. b) Scarp height/throw vs distance profiles for fault F1; the blue plot shows the F1 scarp height measured on multibeam bathymetry; orange plot: seafloor throw measured on seismic profiles; grey plot: LGM throw measured on seismic profiles; the yellow and red lines indicate segment CN and ST respectively. c) and d) Multichannel seismic profile 05 and Sparker profile ST5 across fault F1, respectively. e) and f) Tectono-stratigraphic model proposed for the evolution of the two segments of the fault F1. (For interpretation of the references to color in this figure legend, the reader is referred to the web version of this article.)

4.3.3. The offshore fault system

The offshore fault system includes several subparallel, mostly NE-SW oriented faults dipping toward NW between 450 m and 650 m wd (Figs. 6a and 11); a subordinate set of faults (F7, F24) have an opposite dip. The fault escarpments are 2–8 km long and 2–10 m high, locally showing a staircase morphology. Some escarpments cross-cut the sinuous segment of the Angitola Canyon or minor channels located in the northern area. These faults can be traced on a wide area between the sinuous course of the Angitola Canyon and the base of the upper sector of the continental slope off Capo Suvero (Fig. 6a). The major faults of this system (F15, F20, F24, and F26) have seafloor throws up to 8 m and lengths larger than 6 km (Fig. 6b). Faults F20 and F24 offset the LGM

unconformity with throws of 9.6–12 m. Faults F13 and F15 cross-cut two minor channels carving the continental slope.

5. Discussion

5.1. Fault activity during the post-LGM

Identifying the LGM unconformity, which is a chronostratigraphic marker with a regional extent (e.g., Chiocci et al., 1989; Martorelli et al., 2010a), allowed us to reconstruct faults activity since the LGM. The reconstruction of the timing of activity is optimised for faults located in the continental shelf, where the MFS is also detectable. Multiple scarps
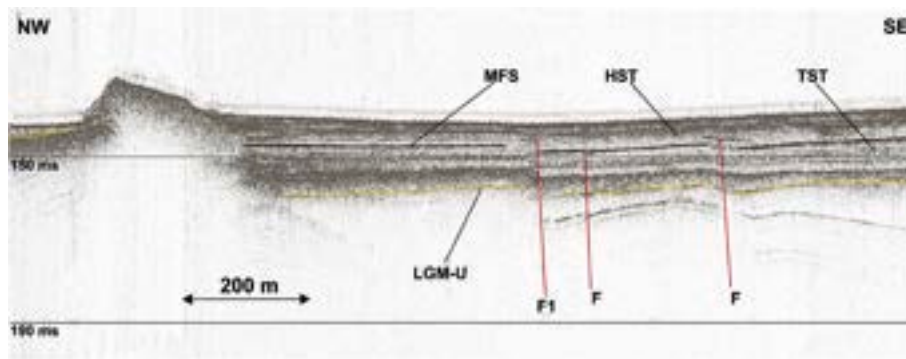
Fig. 8. Chirp profile SE20 across the northern segment of fault F1. See Fig. 1b for location.
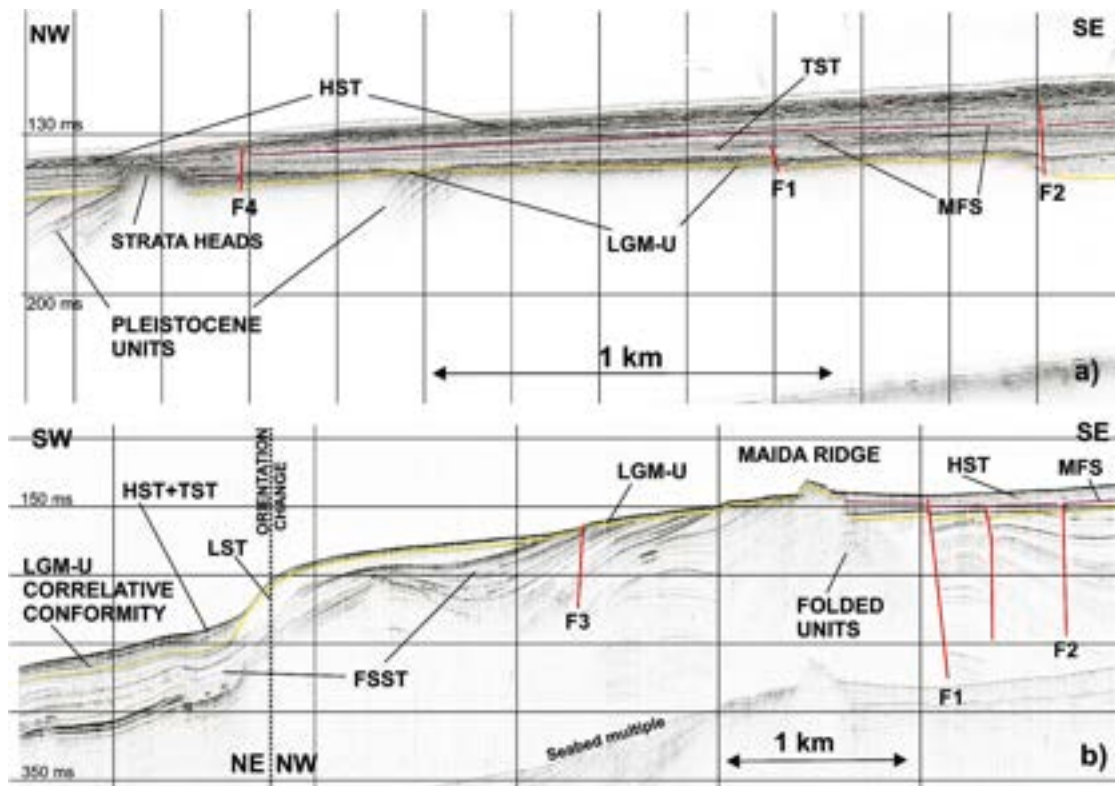

Fig. 9. a) Chirp seismic profile HR2 across faults F1 and F2. b) Sparker seismic profile ST4 across faults F1, F2 and F3. See Fig. 1b for location.

and the increase of downward displacement provide evidence of multiple rupture events. This is the case of fault F1 that, along with the other studied faults, formed in response to the Early Pleistocene-Recent left-lateral transtensional phase that led to the formation of high-angle normal faults above the Maida Ridge (Corradino et al., 2021). Fault F1 shows a longer deformation record during the post-LGM and Holocene as indicated by three ruptures. The detailed morpho-bathymetric analysis of Fault F1 shows a deformation pattern characterised by a well-defined escarpment along the fault trace (Fig. 7a; blue line in Fig. 7b). However, seismic profiles indicate that the fault offsets the seabed only in its central part (orange line in Fig. 7b) where the escarpment is less developed. Based on the new data and interpretation, a tectono-sedimentary model is proposed here to explain the behaviour of this fault. The model considers the evolution of an extensional fault-propagation fold (sensu Sharp et al., 2000) developed in an offshore area with different syntectonic sedimentation rates. In the southern segment of the fault (segment ST, red line in Fig. 7a), the height of the morphological scarp reaches its maximum value (Fig. 7b), whereas the

fault offsets Upper Pleistocene deposits below the reflector R only (marked by the green line in Fig. 7c) and the overlaying deposits are folded. The latter also shows a decreasing inclination of the strata moving upwards (a1 > a2 in Fig. 7c), suggesting that their deposition occurred during fault activity. Conversely, deposits below the reflector R show parallel strata, indicating a deposition before the fault activity. Thicknesses of post-LGM deposits vary from about 5 to 8 m in the footwall, and hanging wall of the fault, respectively (Fig. 7c). Based on the geometric features of the deposits, the southern segment of fault F1 is interpreted as an extensional fault-propagation fold characterised by a slip rate lower than the sedimentation rate (Fig. 7e). The tectonic model we propose to illustrate the evolution of the southern segment of the fault F1 (ST, red line in Fig. 7a) consists of three stages. In the first stage, extensional fault nucleates at depth, and a zone of distributed deformation (e.g., monocline) develops upward (Stage I in Fig. 7e). The syntectonic unit thins toward the footwall, reflecting the variation in accommodation space due to the development of the monocline. Through time the fault propagates upwards with a decreasing
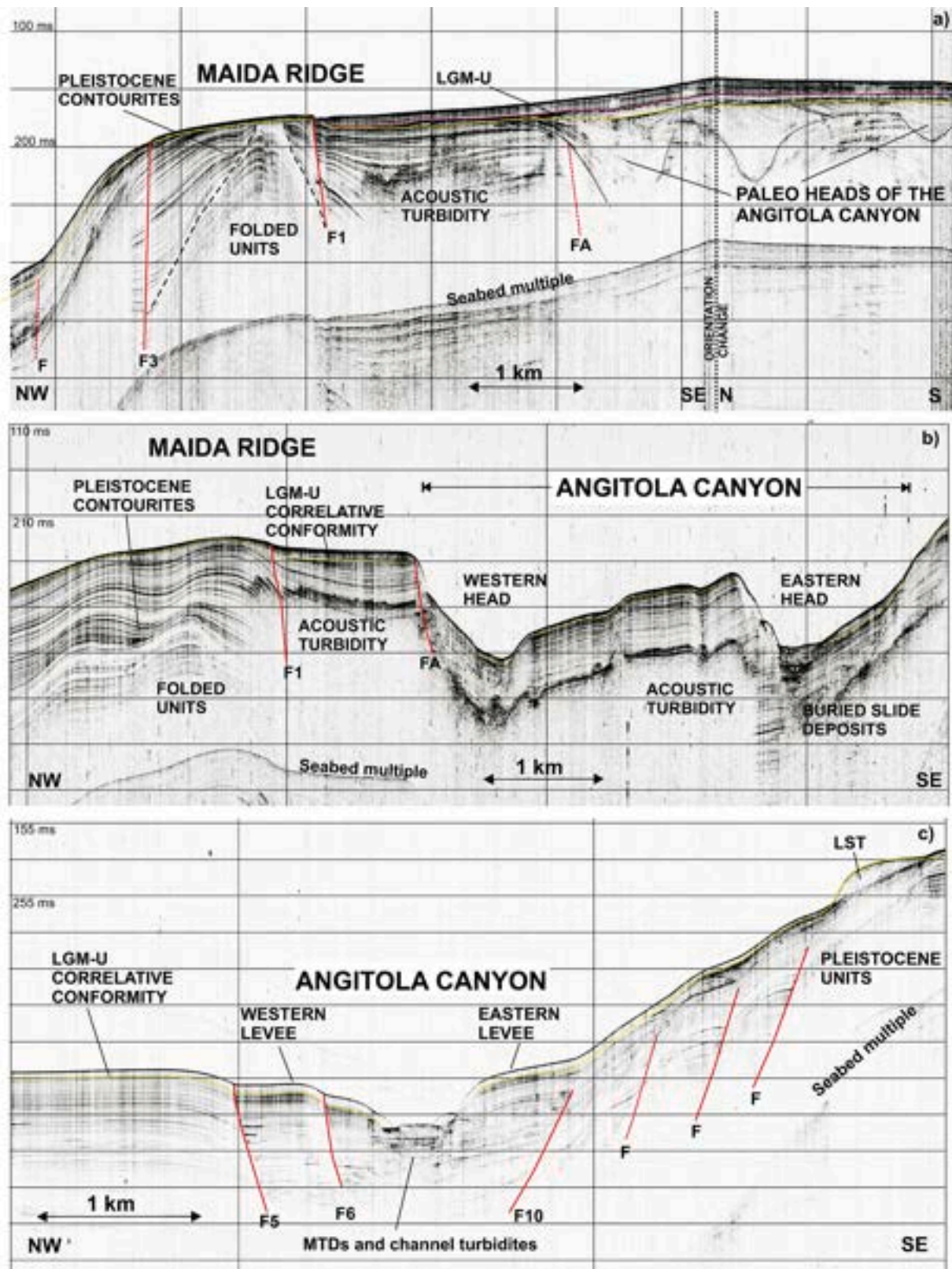
Fig. 10. a) Sparker profile ST5 across the Maida Ridge and the buried head of the Angitola Canyon. b) Sparker profile ST7 across the southern segment of fault F1 and the head of the Angitola Canyon. c) Sparker profile ST9 across the Angitola Canyon showing faults affecting the flanks of the Canyon. See Fig. 1b for location.

displacement, whereas the limb of the monocline steepens. The fault offsets the monocline and part of the syntectonic unit during the second stage. The seafloor is not displaced because the sedimentation rate is greater than the slip rate of the fault. In the final stage, the fault-propagation fold continues to propagate upwards, offsets syntectonic strata, and folds the upper part of the syntectonic unit resulting in the formation of a well-defined escarpment at the sea floor (Stage III in Fig. 7e). This model justifies 1) the decreasing inclination upwards of the
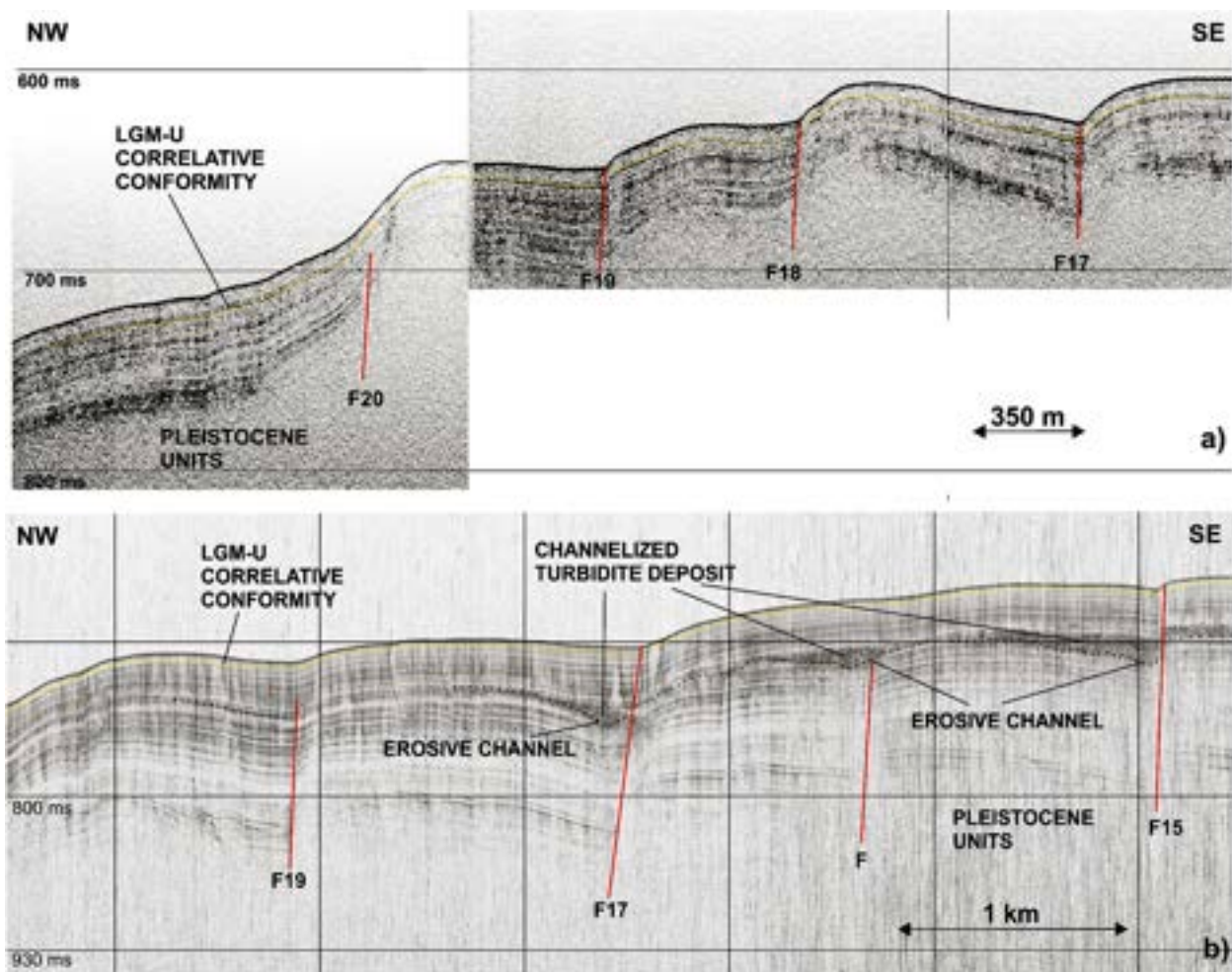
Fig. 11. a) Chirp profile NL68 across faults F17, F18, F19 and F20. b) Sparker profile S. Eufemia_6 across a set of offshore faults (F15, F17, F19). See Fig. 1b for location.

post-Reflector-R syntectonic strata, 2) the difference in sedimentary thickness observed in the footwall and hanging wall of the fault-propagation fold and 3) the escarpment at the seabed. This morpho-structure at the seabed confirms the fault activity, even though no sea-floor offset can be observed in the seismic profiles (Fig. 7c). Differently, the northern and central segment of the fault F1 (CN, yellow line in Fig. 7a) is characterised by a displacement at the seabed or a subsurface rupture (Fig. 7d). The internal pattern of the deposits in the hanging wall of the fault shows a decreasing inclination of the strata upwards, indicating a tectonic control during their deposition (a1 > a2 in Fig. 7d). Also, the post-LGM sediments have a different thickness in the footwall and hanging wall of the fault, varying between 3 and 5 m, respectively (Fig. 7d). These depositional features could be explained by the development of an extensional fault-propagation fold that evolves with a slip rate that becomes greater than the sedimentation rate. The model consists of three stages. During the first stage, the fault affects the deeper strata, and a monocline deforms the upper deposit that thins toward the footwall (Stage I in Fig. 7f), similar to the first stage described above. During Stage II, the fault propagates upwards with a decreasing displacement, cutting the monocline and reaching the lower part of the syntectonic unit. When the sedimentation rate becomes lower than the vertical slip rate, the fault propagates through the whole syntectonic unit and offsets the seafloor (Stage III in Fig. 7f). Minor faults that cut the monocline accommodate the deformation.

The proposed tectonic model allows us to clarify the thickness variation in the footwall and hanging wall of the segment CN of the fault F1, the decreasing displacement of the fault upwards, and the decreasing inclination of the strata of Late Quaternary deposits upwards. Also, it is possible to explain the folded strata close to the fault as remnants of the cut monocline (Fig. 7d and f) and not as the result of drag folds associated with normal faults (Gawthorpe and Hardy, 2002). To validate the proposed model of the extensional fault-propagation fold for the northern and central segments, we have calculated and compared the post-LGM sedimentation rate, which is ~0.15 mm/y in the footwall of the fault F1, with the post-LGM slip rate, which is ~0.24 mm/y. This comparison confirms the model's assumption that the sedimentation rate is lower than the slip rate of the fault. Overall, such model highlights that the interplay between the slip rate and the sedimentation rate may determine a different morpho-sedimentary architecture along the same fault.

On the continental slope, the major faults of the offshore system are F13, F15, F20, F24 and F26 (Fig. 6a). Here, the sedimentation rates are generally lower than in the shelf sector, and chronostratigraphic constraints are less accurate because of the difficulty in identifying the MFS surface and other horizons within the postglacial sequence. However, these faults show high seafloor throws (about 10 m, Fig. 6b) and multiple rupture events, indicating again a relatively long-term activity. In particular, finding a well developed array of faults suggests the linkage of fault segments that produce deformation localized in significant through-going faults (Cowie, 1998). Moreover, some of these faults (e.g., F13 and F26) show the maximum throw close to their termination, indicating truncation by successive faulting or erosive processes related

to the activity of the Angitola Canyon (e.g., the south-western segment of F26; Fig. 12).

5.2. Tectonic control on morpho-sedimentary processes

Several lines of evidence suggest that tectonic activity controlled or influenced recent geomorphic and sedimentary processes in the SEG. On a broad scale this is indicated, for example, by the narrow width of the shelf (<10 km), high slope gradients (>1–1.5°) and variable shelf break depth (140–170 m). Moreover, tectonics exerted a primary morphological control through the development of main reliefs (e.g., the Maida Ridge; Fig. 12). The Angitola Canyon provides a further example. In this case, the alignment and proximity of the canyon with fault escarpments (Fig. 12), indicate that it developed along traces of major faults and its position has been locally constrained by structurally-generated ridges (i. e., the Maida Ridge) and possibly influenced by the Briatico fault escarpment (Fig. 12). On a smaller spatial scale, a prominent tectonic control is indeed documented by the fault scarps observed at the seabed.

In addition to the control exerted on the SEG morphology, a variety of processes are likely influenced by tectonic activity, such as gravitative processes (e.g., landsliding), sedimentary processes (e.g., sediment accumulation rates, stratigraphic architecture and canyon-channels development), fluid migration and seepage. This is suggested by the spatial distribution of different morpho-sedimentary features (e.g., slides and pockmarks) that is not random but typically connected to main faults (Fig. 12). Particular patterns of sediment accumulation provide further indication (e.g., hanging wall channelised turbidites). In the following, we illustrate and discuss the primary evidence of the influence of tectonic activity on sedimentation, slope instability and fluid migration.

5.2.1. Influence on sedimentation and depositional systems

In the SEG, sedimentation rates and stratal patterns are influenced by fault activity as indicated, for example, by thickness variation across almost all the studied faults (i.e., post-LGM thickening up to 100 % in the F1 hanging wall sector; Figs. 5c and 12), which may create local depocentres at the centre of the faults (Cowie et al., 2000). Moreover, on the continental shelf, narrow depocentres of the TST deposits are elongated NNE-SSW (Martorelli et al., 2010a), parallel to the strike of fault F2,

suggesting a tectonic control on their deposition (Leeder, 2011). Overall, these findings reflect the synsedimentary nature of the faults (Cowie et al., 2000). Differently, in some cases, fault activity creates very steep seabed escarpments that represent bypass zone for sedimentation (the Briatico fault, Fig. 12). Examples of stratal patterns influenced by tectonic activity include: 1) step-like stratigraphy (Figs. 11 and 12) typically determined by faults of the offshore system; 2) scarps, strata dip and tilting (faults F24, F18, F2 in the subsurface); 3) extensional drag folded strata (e.g., faults F5 and F6 bordering the Angitola Canyon; Fig. 12) and down-section increase in reflector dip (e.g., F17).

Interestingly, there is also evidence that tectonic activity influenced the characteristics of turbidite and contourite depositional systems and their elements. Examples are provided by morphological characteristics of various elements of the Angitola Canyon system, such as the shape and position of its head, the linear shape of its flanks and abrupt sinuosity changes (Fig. 12). In particular, the linear shape of the two branches forming the canyon head is determined by faults oriented along NE-SW and E-W (e.g., fault F6 in the case of the northern branch). Similarly, both the canyon flanks have a straight and segmented trend mostly related to the development of F5, F6 and F11 fault planes that confine the straight segment of the Angitola Canyon (Figs. 10c and 12). The Angitola Canyon starts a meandering path when it intercepts faults F8, F7, F25; a knickpoint is observed upslope fault F8 (Figs. 2c and 12). Furthermore, F24 possibly controlled the adjacent Angitola meander. Finally, as reported by Corradino et al. (2021), the Angitola Canyon underwent differential uplift below and above 510 m wd, likely due to the topographic response to the Late Quaternary activity of the Maida Ridge. All these findings suggest a primary tectonic control on the characteristics of the canyon system and its plan-view morphology. These observations are similar to those described along other tectonically active margins (e.g., Greene et al., 1991; Chiang and Yu, 2006; Micallef et al., 2014; Soutter et al., 2021). In particular, the location and planform canyon shape seem to be confirmed as a marked indication of active deformation, as also revealed from the nearby Gioia-Mesima Canyon-Channel system (Morelli et al., 2022), the Cook Strait Canyon (Micallef et al., 2014) and the Esmeraldas Canyon (Collot et al., 2019).

Further evidence of fault control in the development of channelised turbidite systems are related to the characteristic of some minor slope channels. Examples include:
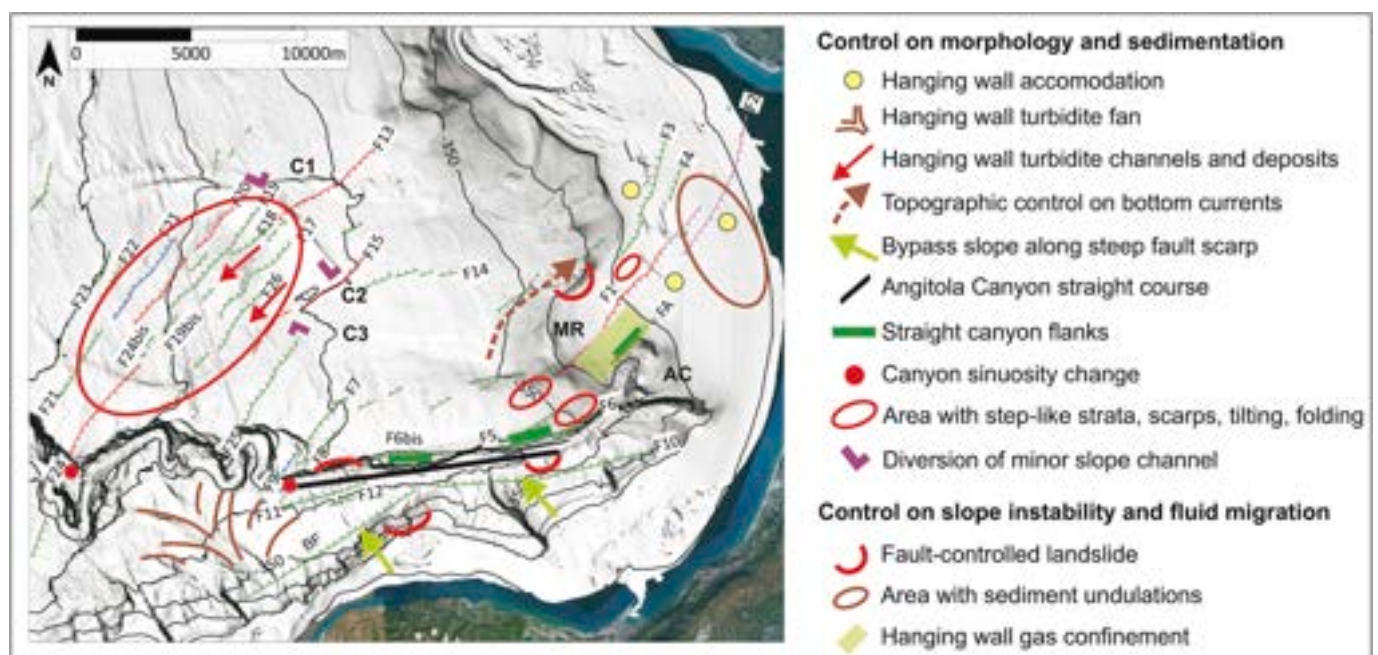

Fig. 12. Sketch of the main morpho-sedimentary features controlled by fault activity.

1) the abrupt change of the course of slope channel C1 observed at the northern tip of the offshore ridge close to faults F19 and F20 and the abrupt change observed in the course of slope channel C3 (Fig. 12);

2) thick sediment accumulation of turbidite fan deposits in the down-thrown side of the Briatico fault, with superimposed upper-flow regime bedforms (Figs. 3c and 12). Here, the development of supercritical bedforms is possibly favored by steep gradients and (mainly) slope breaks inherited by fault activity (e.g., Kostic, 2011);

3) localized accumulation of channelised coarse-grained sediment, likely associated with channelised turbidite deposits (e.g., Mayall et al., 2006), within the upper part of Pleistocene deposits in the downthrown side of offshore faults (e.g., F15 and F17 in Fig. 11). Such configuration highlights the primary effect of topographic steering on turbidity current pathways exerted by tectonic troughs (Leeder, 2011).

Finally, a local morpho-structural control can be envisaged also for the deposition of contourites on the NW flank of the Maida Ridge (Figs. 10a and 12). These deposits testify to the activity of along-slope bottom currents, topographically steered by the relief of this structural high (e.g., Martorelli et al., 2010b; Falcini et al., 2016). The finding of a significant topographic steering for turbidite flows and bottom currents developed in the SEG strengthens the role of the topographic control on these different sedimentary flows in tectonically controlled margins (e.g., Lomas and Joseph, 2004; Rebesco and Camerlenghi, 2008; Liu et al., 2021). Overall, most of these findings are consistent with the role of fault array evolution for patterns of sediment dispersal, depositional systems and stratigraphic architecture observed in extensional settings (e.g., Gupta et al., 1998; Dawers and Underhill, 2000).

5.2.2. Influence on gravitative processes and fluid migration and seepage

Among the several slide scars and slide deposits recognised in the study area, the development of the S. Eufemia slide and the slides located along the flanks of the Angitola Canyon is likely controlled by the activity of faults (Fig. 12). This is suggested by the close spatial correspondence between landslide scars and faults scarps (e.g., the uppermost portion of the S. Eufemia slide scar is adjacent to fault F3 and the set of scars affecting the northern flank of the Angitola Canyon is adjacent to F6bis). In both these cases, high slope gradients and weakened sediment might represent predisposing conditions determined by fault activity. Earthquakes and focused ground motion along active faults likely represented triggering factors. This is also because the landslides are located in deep water, where the role of storm waves can be excluded (e.g., Kluesner et al., 2020; Watson et al., 2020). Moreover, tectonically inherited morphologies locally controlled the distribution of landslide deposits, as indicated by the paleolandslide deposits accumulated in the topographic low confined by the offshore mounded relief created by transpressional tectonics from the Early Pliocene to Early Pleistocene (Corradino et al., 2021; Fig. 12). A similar configuration has been described for major landslide deposits (the Pleistocene Suvero slide deposits) that accumulated in the nearby Paola Basin (Trincardi and Normark, 1989). This suggests that the limited runout of the failing mass by intraslope reliefs is a common characteristic of this sector of the Calabro-Tyrrhenian margin. A further relation with gravitative processes is suggested by sediment undulations observed in the sector displaced by faults F1, F2 and F4. Under the assumption that these sediment undulations result from creep processes (see Section 4.1.4), sediment deformation may be influenced by fault activity and seismicity. Here, creep deformation could also be favored by high thickness (>8 m) of highstand muddy sediment and occurrence of fluid-charged sediments. Finally, a local relation between faults and fluid migration and seepage is observed along fault F1. Here features related to fluids are recognised both in the subsurface (acoustic turbidity zones) and at the seabed (pockmarks). Seismic profiles show that fault F1 locally represents a barrier for lateral fluid migration, confining the fluids in the hanging wall side (Figs. 10 and 12). However, the fault plane locally

allows the seepage of fluids, as testified by the alignment of pockmarks along its trace (Fig. 4). This highlights a local higher permeability, possibly reflecting structural complexity (Eichhubl et al., 2009).

5.3. Controlling factors in margin shaping

The distinctive signature that tectonic activity leaves on morpho-sedimentary features and processes revealed by this study indicates a prominent influence of tectonics in shaping the SEG margin. However, also non-tectonic controlling factors (e.g., glacio-eustatic sea level changes and sediment supply) significantly concur in margin shaping (e.g., Gawthorpe and Leeder, 2000; Leeder, 2011; Mestdagh et al., 2019). For example, they determine major changes in sedimentation patterns and stratigraphic architecture (e.g., Maestro et al., 2013; Matenco and Haq, 2020). Indeed, the SEG margin is largely controlled by the background influence of glacio-eustatic sea-level changes, but previous studies (Chiocci et al., 1989; Chiocci and Orlando, 1995; Martorelli et al., 2010a) have also shown the influence of spatial heterogeneity in sediment supply. In particular, the complex geology of the Tyrrhenian margin of the Calabrian Arc determines the high amount of sediment supplied to the margin and its variability at even small (e.g., km's) spatial scale. Such variability typically influences gradients, sediment type, slope stability, sedimentary processes and formation of depocentres (Pettinga and Jobe, 2020), thus determining a key role in shaping the margin. A further example of the spatial variability of non-tectonic factors is the oceanographic regime and activity of contourite-related bottom currents, which control erosive-depositional processes and sediment distribution, interacting with the paleo-seabed topography, and thus favoring the local accumulation of contourite deposits (this study; Amelio and Martorelli, 2008; Martorelli et al., 2010b). All this indicates that multiple factors, such as: tectonics, glacio-eustatic sea-level changes, sediment supply, instability processes and bottom currents drive the SEG margin shaping. The prevalence of one or various processes in a particular area and the resulting morpho-sedimentary architecture is determined by their interplay during a specific time period.

Although we are able to distinguish the main controlling factors, the disclosure of their influence in margin shaping through time is however still inhibited by the extreme variability of their magnitude and impact through time (e.g., García et al., 2020). For example, sediment supply, bottom currents and sediment gravity flows are intimately related to Late-Quaternary climate and sea-level changes (e.g., García et al., 2020; Martorelli et al., 2021; Ercilla et al., 2021, respectively). This determines a further complicated interplay, within which the role of a specific factor can be amplified, and a single process may become dominant (e.g., the dominance of sediment gravity flows during sea level lowstands) or faded (e.g., weakening of contourite-related bottom currents during warm climatic phases in the Mediterranean; e.g., Martorelli et al., 2021). In this respect, additional information (e.g., chronostratigraphic data) and a source-to-sink approach would help the accurate definition of their influence through time.

6. Conclusions

This study presents the first comprehensive analysis of morpho-sedimentary features of the S. Eufemia Gulf and their interaction with tectonic features, based on the interpretation of an extensive dataset, including very high-resolution multibeam bathymetry, backscatter data and seismic profiles. A series of active faults were documented in the upper part of Late Quaternary deposits. On the shelf, high sedimentation rates during the Late Quaternary and well-defined chronostratigraphic markers allowed a detailed reconstruction of fault activity since the LGM. Among the active faults, one of the most prominent structures is the fault F1 that extends across the continental shelf and the upper continental slope. This fault is characterised by two main segments: a segment characterised by seafloor deformation with metric slip or by

shallow deformation affecting Holocene deposits; a sector characterised by folding of the seafloor. A combined tectono-stratigraphic model of an extensional fault propagation fold is proposed to explain such deformation. The proposed model shows that when the sedimentation rate is lower than the slip rate, the fault cut the syntectonic unit, reaching the seabed. Conversely, when the sedimentation rate is greater than the slip rate of the fault, deformation propagates upwards as a fold. The fault is active in this second case too, even if the seabed is not cut.

Furthermore, results from this study indicate that tectonic deformation determined by active faults leaves a prominent geomorphological expression at the seabed and on recent sedimentary processes. A scheme of the main morpho-sedimentary features controlled or influenced by tectonic activity during the Late-Quaternary is proposed to disentangle the complex interaction with the various morpho-sedimentary processes active in the SEG. In addition to the formation of several linear escarpments, the activity of the faults influenced sedimentation rates, determining hanging wall accommodation and controlling stratal patterns. Locally, it controlled the spatial distribution of contourite and turbidite depositional systems, in particular influencing the course and morphology of the upper reach of the Angitola Canyon and of minor slope-channels. Moreover, it also influenced the distribution of various landslides and fluid migration (e.g., hanging wall gas confinement).

These findings make the SEG a relevant active sector of the southeastern Tyrrhenian continental margin, because a clear link between fault activity and submarine morpho-sedimentary processes shaping the margin has been barely documented, despite its recent origin and active tectonic deformation. Overall, the high variability of geomorphic signature documented in this study increases our knowledge on the morpho-sedimentary response to active tectonics, highlighting the potential of high-resolution morpho-stratigraphic studies within the field of submarine tectonic geomorphology.

Besides the extensive impact of tectonic activity on morpho-sedimentary processes recognised in the SEG, other non-tectonic controlling factors (i.e., glacio-eustatic sea level changes, sediment supply, activity of bottom currents) concur in margin shaping. A complex interplay of these factors can be envisaged during the Late-Quaternary climate and sea-level changes.

Supplementary data to this article can be found online at https://doi.org/10.1016/j.geomorph.2023.108775.

CRediT authorship contribution statement

Martorelli E. Conceived and designed the study, collected the data, performed the processing of seismic data, performed the analysis of multibeam, seismic and structural data, wrote the paper. Casalbore D. Collected the data, performed the analysis of multibeam and seismic data, wrote part of the paper. Bosman A. Collected the data, performed the processing and analysis of Multibeam-backscatter data, wrote part of the paper. Pepe F. Collected the data, performed the processing of seismic data and the analysis of structural data, wrote part of the paper. Corradino M. Collected the data, performed the analysis of structural data, wrote part of the paper. de Nardis R. Performed the analysis of seismic data wrote part of the paper. Monaco C. Performed the analysis of structural data and wrote part of the paper. Sposato A. Collected the data, performed the analysis of seismic data and wrote part of the paper.

Declaration of competing interest

The authors declare that they have no known competing financial interests or personal relationships that could have appeared to influence the work reported in this paper.

Data availability

Data will be made available on request.

References

Allen, P.A., 2008. From landscapes into geological history. Nature 451 (7176), 274–276.
Allen, P.A., Allen, J.R., 2013. Basin Analysis: Principles and Application to Petroleum Play Assessment. John Wiley & Sons.
Amelio, M., Martorelli, E., 2008. Seismo-stratigraphic characters of paleocontourites along the Calabro-Tyrrhenian margin (Southern Tyrrhenian Sea). Mar. Geol. 252 (3–4), 141–149.
Barreca, G., Scarfì, L., Gross, F., Monaco, C., De Guidi, G., 2019. Fault pattern and seismotectonic potential at the south-western edge of the Ionian Subduction system (southern Italy): new field and geophysical constraints. Tectonophysics 761, 31–45.
Basili, R., Burrato, P., De Santis, G.M., Fracassi, U., Maesano, F.E., Tarabusi, G., Tiberti, M.M., Vallone, R., Vannoli, P., DISS Work. Group, 2021. Database of Individual Seismogenic Sources (DISS), Version 3.3.0: A Compilation of Potential Sources for Earthquakes Larger Than M 5.5 in Italy and Surrounding Areas.
Bosman, A., Casalbore, D., Anzidei, M., Muccini, F., Carmisciano, C., 2015. The first ultra-high resolution Marine Digital Terrain Model of the shallow-water sector around Lipari Island (Aeolian archipelago, Italy). Ann. Geophys. https://doi.org/10.4401/ag-6746.
Bosman, A., Romagnoli, C., Madricardo, F., Correggiari, A., Fogarin, S., Trincardi, F., 2020. Short-term evolution of Po della Pila delta lobe from high-resolution multibeam bathymetry (2013-2016). Estuar. Coast. Shelf Sci. 233, 106533.
Brutto, F., Muto, F., Loreto, M.F., De Paola, N., Tripodi, V., Critelli, S., Facchin, L., 2016. The Neogene-Quaternary geodynamic evolution of the central Calabrian Arc: a case study from the western Catanzaro Trough basin. J. Geodyn. 102, 95–114.
Burbank, D.W., Anderson, R.S., 2001. Geomorphic markers. In: Malden (Ed.), Tectonic Geomorphology. Blackwell Publishing, pp. 13–32.
Casalbore, D., Bosman, A., Ridente, D., Chiocci, F.L., 2014. Coastal and submarine landslides in the tectonically-active Tyrrhenian Calabrian Margin (southern Italy): examples and geohazard implications. In Submarine mass movements and their consequences. Adv. Nat. Technol. Hazards Res. 37, 261–269.
Chiang, C.S., Yu, H.S., 2006. Morphotectonics and incision of the Kaoping submarine canyon, SW Taiwan orogenic wedge. Geomorphology 80 (3–4), 199–213.
Chiocci, F.L., Orlando, L., 1995. Effects of Pleistocene sea level changes on a highly deforming continental margin, Calabrian shelf, Italy. Boll. Geofis. Teor. Appl. 37, 39–58.
Chiocci, F.L., Orlando, L., 1996. Lowstand terraces on Tyrrhenian Sea steep continental slopes. Mar. Geol. 134 (1–2), 127–143.
Chiocci, F.L., D'Angelo, S., Orlando, L., Pantaleone, A., 1989. Evolution of the Holocene shelf sedimentation defined by high resolution seismic stratigraphy and sequence analysis (Calabro-Tyrrhenian continental shelf). Mem. Soc. Geol. Ital. 48, 359–380.
Collot, J.Y., Ratzov, G., Silva, P., Proust, J.N., Migeon, S., Hernandez, M.J., et al., 2019. The Esmeraldas Canyon: a helpful marker of the Pliocene-Pleistocene tectonic deformation of the North Ecuador southwest Colombia conver-gent margin. Tectonics 38, 3140–3166.
Corradino, M., Pepe, F., Bertotti, G., Picotti, V., Monaco, C., Nicolich, R., 2020. 3D architecture and Plio-Quaternary evolution of the Paola Basin: insights into the forearc of the Tyrrhenian-Ionian subduction system. Tectonics 39 (2), e2019TC005898.
Corradino, M., Pepe, F., Burrato, P., Kanari, M., Parrino, N., Bertotti, G., Bosman, A., Casalbore, D., Ferranti, L., Martorelli, E., Monaco, C., Sacchi, M., Tibor, G., 2021. An integrated multiscale method for the characterisation of active faults in offshore areas. The case of Sant'Eufemia Gulf (Offshore Calabria, Italy). Front. Earth Sci. 9, 476.
Corradino, M., Morelli, D., Ceramicola, S., Scarfì, L., Barberi, G., Monaco, C., Pepe, F., 2023. Active tectonics in the Calabrian Arc: insights from the Late Miocene to Recent structural evolution of the Squillace Basin (offshore eastern Calabria). Tectonophysics 851, 229772.
Cowie, P.A., 1998. A healing–reloading feedback control on the growth rate of seismogenic faults. J. Struct. Geol. 20 (8), 1075–1087.
Cowie, P.A., Gupta, S., Dawers, N.H., 2000. Implications of fault array evolution for synrift depocentre development: insights from a numerical fault growth model. Basin Res. 12 (3–4), 241–261.
Cultrera, F., Barreca, G., Burrato, P., Ferranti, L., Monaco, C., Passaro, S., Pepe, F., Scarfì, L., 2017. Active faulting and continental slope instability in the Gulf of Patti (Tyrrhenian side of NE Sicily, Italy): a field, marine and seismological joint analysis. Nat. Hazards 86 (2), 253–272.
Dawers, N.H., Underhill, J.R., 2000. The role of fault interaction and linkage in controlling synrift stratigraphic sequences: Late Jurassic, Statfjord East area, northern North Sea. AAPG Bull. 84 (1), 45–64.

De Ritis, R., Pepe, F., Orecchio, B., Casalbore, D., Bosman, A., Chiappini, M., Chiocci, F., Corradino, M., Nicolich, R., Martorelli, E., Monaco, C., 2019. Magmatism along lateral slab edges: insights from the Diamante-Enotrio-Ovidio volcanic-intrusive complex (Southern Tyrrhenian Sea). Tectonics 38 (8), 2581–2605.

Del Ben, A., Barnaba, C., Taboga, A., 2008. Strike-slip systems as the main tectonic features in the Plio-Quaternary kinematics of the Calabrian Arc. Mar. Geophys. Res. 29 (1), 1–12.

Eichhubl, P., Davatz, N.C., Becker, S.P., 2009. Structural and diagenetic control of fluid migration and cementation along the Moab fault, Utah. AAPG Bull. 93 (5), 653–681.

Ercilla, G., Casas, D., Estrada, F., Vázquez, J.T., Iglesias, J., García, M., Gómez, M., Acosta, J., Gallart, J., Maestro-González, A., Team, M, 2008. Morphosedimentary features and recent depositional architectural model of the Cantabrian continental margin. Mar. Geol. 247 (1–2), 61–83.

Ercilla, G., Vázquez, J.T., Alonso, B., Bárcenas, P., Casas, D., d'Acremont, E., Estrada, F., Fernández-Salas, L.M., Galindo-Zaldívar, J., Juan, C., Lobo, F., López-González, N., Palomino, D., Sánchez-Guillamón, O., Chourak, M., Gil, A., Gómez-Ballesteros, M., El Moumni, B., Peláez, J.A., Valencia, J., Gorini, C., 2021. Seafloor morphology and processes in the Alboran Sea. In: Alboran Sea-Ecosystems and Marine Resources. Springer, Cham, pp. 157–205.

Falcini, F., Martorelli, E., Chiocci, F.L., Salusti, E., 2016. A general theory for the effect of local topographic unevenness on contourite deposition around marine capes: an inverse problem applied to the Italian continental margin (Cape Suvero). Mar. Geol. 378, 74–80.

Ferranti, L., Santoro, E., Mazzella, M.E., Monaco, C., Morelli, D., 2009. Active transpression in the northern Calabria Apennines, southern Italy. Tectonophysics 476 (1–2), 226–251.

Ferranti, L., Burrato, P., Pepe, F., Santoro, E., Mazzella, M.E., Morelli, D., Passaro, S., Vannucci, G., 2014. An active oblique contractional belt at the transition between the Southern Apennines and Calabrian Arc: the Amendolara Ridge, Ionian Sea, Italy. Tectonics 33 (11), 2169–2194.

Ferranti, L., Pepe, F., Barreca, G., Meccariello, M., Monaco, C., 2019. Multi-temporal tectonic evolution of Capo Granitola and Sciacca foreland transcurrent faults (Sicily Channel). Tectonophysics 765, 187–204.

Galli, P., Molin, D., 2009. Il terremoto del 1905 in Calabria: Revisione della distribuzione degli effetti e delle ipotesi sismogenetiche, Il Quaternario-Ital. J. Quat. Sci. 22 (2), 207–234.

Gamberi, F., Marani, M., 2007. Downstream evolution of the Stromboli slope valley (south-eastern Tyrrhenian Sea). Mar. Geol. 243 (1–4), 180–199.

García, M., Llave, E., Hernández-Molina, F.J., Lobo, F.J., Ercilla, G., Alonso, B., Casas, D., Mena, A., Fernández-Salas, L.M., 2020. The role of late Quaternary tectonic activity and sea-level changes on sedimentary processes interaction in the Gulf of Cadiz upper-middle continental slope (SW Iberia). Mar. Pet. Geol. 121, 104595.

Gawthorpe, R., Hardy, S., 2002. Extensional fault-propagation folding and base-level change as controls on growth-strata geometries. Sediment. Geol. 146 (1–2), 47–56.

Gawthorpe, R.L., Leeder, M.R., 2000. Tectono-sedimentary evolution of active extensional basins. Basin Res. 12 (3–4), 195–218.

Geist, E.L., 2000. Origin of the 17 July 1998 Papua New Guinea tsunami: earthquake or landslide. Seismol. Res. Lett. 71 (3), 344–351.

Greene, H.G., Clarke Jr., S.H., Kennedy, M.P., 1991. Tectonic evolution of submarine canyons along the California continental margin. From shoreline to abyss. In: SEPM Sp. Publ. 46.

Gupta, S., Cowie, P.A., Dawers, N.H., Underhill, J.R., 1998. A mechanism to explain rift-basin subsidence and stratigraphic patterns through fault-array evolution. Geology 26 (7), 595–598.

Hernandez-Molina, F., Somoza, J., Lobo, I., F., 2000. Seismic stratigraphy of the Gulf of Cadiz continental shelf: a model for late Quaternary very high resolution sequence stratigraphy and response to sea-level fall. In: Hunt, D.E., Gawthorpe, R.L. (Eds.), Sedimentary Responses to Forced Regressions, Geol. Soc., London, Spec. Publ., vol. 172, pp. 329–362.

Hovland, M., Judd, A.G., 1988. Seabed Pockmarks and Seepages: Impact on Geology, Biology and the Marine Environment, vol. 293. Graham & Trotman, London.

Jacques, E., Monaco, C., Tapponnier, P., Tortorici, L., Winter, T., 2001. Faulting and earthquake triggering during the 1783 Calabria seismic sequence. Geophys. J. Int. 147, 499–516.

Kluesner, J.W., Brothers, D.S., Wright, A.L., Johnson, S.Y., 2020. Structural controls on slope failure within the Western Santa Barbara Channel based on 2D and 3D seismic imaging. Geochem. Geophys. Geosyst. 21 (8), e2020GC009055.

Kostic, S., 2011. Modeling of submarine cyclic steps: controls on their formation, migration, and architecture. Geosphere 7 (2), 294–304.

Kostic, S., 2014. Upper flow regime bedforms on levees and continental slopes: turbidity current flow dynamics in response to fine-grained sediment waves. Geosphere 10 (6), 1094–1103.

Lambeck, K., Antonioli, F., Anzidei, M., Ferranti, L., Leoni, G., Scicchitano, G., Silenzi, S., 2011. Sea level change along the Italian coast during the Holocene and projections for the future. Quat. Int. 232 (1–2), 250–257.

Laursen, J., Normark, W.R., 2002. Late Quaternary evolution of the San Antonio Submarine Canyon in the central Chile forearc (~33 S). Mar. Geol. 188 (3–4), 365–390.

Le Dantec, N., Hogarth, L.J., Driscoll, N.W., Babcock, J.M., Barnhardt, W.A., Schwab, W.C., 2010. Tectonic controls on nearshore sediment accumulation and submarine canyon morphology offshore La Jolla, Southern California. Mar. Geol. 268 (1–4), 115–128.

Leeder, M.R., 2011. Tectonic sedimentology: sediment systems deciphering global to local tectonics. Sedimentology 58 (1), 2–56.

Lericolais, G., Berné, S., Féniès, H., 2001. Seaward pinching out and internal stratigraphy of the Gironde incised valley on the shelf (Bay of Biscay). Mar. Geol. 175 (1–4), 183–197.

Liu, S., Hernández-Molina, F.J., Lei, Z., Duarte, D., Chen, H., Wang, C., Lei, Y., Zhuo, H., Huang, S., Zhang, L., Su, M., 2021. Fault-controlled contourite drifts in the southern South China Sea: tectonic, oceanographic, and conceptual implications. Mar. Geol. 433, 106420.

Confined turbidite systems. In: Lomas, S.A., Joseph, P. (Eds.), 2004. Geological Society of London. Spec. Publ. 222.

Loreto, M.F., Fracassi, U., Franzo, A., Del Negro, P., Zgur, F., Facchin, L., 2013. Approaching the seismogenic source of the Calabria 8 September 1905 earthquake: new geophysical, geological and biochemical data from the S. Eufemia Gulf (S Italy). Mar. Geol. 343, 62–75.

Loreto, M.F., Pepe, F., De Ritis, R., Ventura, G., Ferrante, V., Speranza, F., Tomini, I., Sacchi, M., 2015. Geophysical investigation of Pleistocene volcanism and tectonics offshore Capo Vaticano (Calabria, SE Tyrrhenian Sea). J. Geodyn. 90, 71–86.

Loreto, M.F., Pagnoni, G., Pettenati, F., Armigliato, S., Tinti, D., Sandron, F., Brutto, F., Muto, L. Facchin, Zgur, F., 2017. Reconstructed seismic and tsunami scenarios of the 1905 Calabria earthquake (SE Tyrrhenian sea) as a tool for geohazard assessment. Eng. Geol. 224, 1–14.

Maestro, A., López-Martínez, J., Llave, E., Bohoyo, F., Acosta, J., Hernández-Molina, F.J., Munoz, A., Jané, G., 2013. Geomorphology of the Iberian continental margin. Geomorphology 196, 13–35.

Martorelli, E., Chiocci, F.L., Orlando, L., 2010a. Imaging continental shelf shallow stratigraphy by using different high-resolution seismic sources: an example from the Calabro-Tyrrhenian Margin (Mediterranean Sea). Braz. J. Oceanogr. 58, 55–66.

Martorelli, E., Falcini, F., Salusti, E., Chiocci, F.L., 2010b. Analysis and modeling of contourite drifts and contour currents off promontories in the Italian Seas (Mediterranean Sea). Mar. Geol. 278 (1–4), 19–30.

Martorelli, E., Bosman, A., Casalbore, D., Chiocci, F., Conte, A.M., Di Bella, L., Ercilla, G., Falcini, F., Falco, P., Frezza, V., Gaglianone, G., Giaccio, B., Mancini, M., 2021. Mid-to-late Holocene upper slope contourite deposits off Capo Vaticano (Mediterranean Sea): high-resolution record of contourite cyclicity, bottom current variability and sandy facies. Mar. Geol. 431, 106372.

Martorelli, E., Casalbore, D., Falcini, F., Bosman, A., Falese, F.G., Chiocci, F.L., 2022. Large and medium-scale morpho-sedimentary features of the Messina Strait: insights on bottom-current controlled sedimentation and interaction with downslope processes. In: Geological Society, London, Special Publications, p. 523.

Matenco, L.C., Haq, B.U., 2020. Multi-scale depositional successions in tectonic settings. Earth Sci. Rev. 200, 102991 https://doi.org/10.1016/j.earscirev.2019.102991.

Mattei, M., Cifelli, F., D'agostino, N., 2007. The Evolution of the Calabrian Arc: evidence from paleomagnetic and GPS observations. Earth Planet. Sci. Lett. 263, 259–274. https://doi.org/10.1016/j.epsl.2007.08.034.

Mayall, M., Jones, E., Casey, M., 2006. Turbidite channel reservoirs—key elements in facies prediction and effective development. Mar. Pet. Geol. 23 (8), 821–841.

Mestdagh, T., Lobo, F.J., Llave, E., Hernández-Molina, F.J., Van Rooij, D., 2019. Review of the late Quaternary stratigraphy of the northern Gulf of Cadiz continental margin: new insights into controlling factors and global implications. Earth Sci. Rev. 198, 102944.

Micallef, A., Mountjoy, J.J., Barnes, P.M., Canals, M., Lastras, G., 2014. Geomorphic response of submarine canyons to tectonic activity: insights from the Cook Strait canyon system. New Zealand. Geosphere 10 (5), 905–929.

Milia, A., Turco, E., Pierantoni, P.P., Schettino, A., 2009. Four-dimensional tectono-stratigraphic evolution of the Southeastern peri-Tyrrhenian Basins (Margin of Calabria, Italy). Tectonophysics 476 (1–2), 41–56.

Monaco, C., Tortorici, L., 2000. Active faulting in the Calabrian arc and eastern Sicily. J. Geodyn. 29 (3–5), 407–424.

Monaco, C., Tortorici, L., Paltrinieri, W., 1998. Structural evolution of the Lucanian Apennines, southern Italy. J. Struct. Geol. 20 (5), 617–638.

Morelli, E., Martorelli, E., Casalbore, D., Chiocci, F.L., 2022. Morpho-stratigraphic evolution of a tectonically controlled canyon-channel system in the Gioia Basin (Southern Tyrrhenian Sea). Mar. Geol. 451, 106881.

Pepe, F., Bertotti, G., Ferranti, L., Sacchi, M., Collura, A.M., Passaro, S., Sulli, A., 2014. Pattern and rate of post-20 ka vertical tectonic motion around the Capo Vaticano Promontory (W Calabria, Italy) based on offshore geomorphological indicators. Quat. Int. 332, 85–98.

Pettinga, L.A., Jobe, Z.R., 2020. How submarine channels (re) shape continental margins. J. Sediment. Res. 90 (11), 1581–1600.

Pickering, K.T., Hiscott, R.N., 2016. Deep Marine Systems. Processes, Deposits, Environments, Tectonics and Sedimentation. AGU and Wiley (657 pp.).

Piper, D.J., Cochonat, P., Morrison, M.L., 1999. The sequence of events around the epicentre of the 1929 Grand Banks earthquake: initiation of debris flows and turbidity current inferred from side scan sonar. Sedimentology 46, 79–97.

Pirrotta, C., Barberi, G., Barreca, G., Brighenti, F., Carnemolla, F., De Guidi, G., Monaco, C., Pepe, F., Scarfì, L., 2021. Recent activity and kinematics of the bounding faults of the Catanzaro Trough (Central Calabria, Italy): new morphotectonic, geodetic and seismological data. Geosciences 11 (10), 405.

Pirrotta, C., Parrino, N., Pepe, F., Tansi, C., Monaco, C., 2022. Geomorphological and morphometric analyses of the Catanzaro Trough (Central Calabrian Arc, Southern Italy): seismotectonic implications. Geosciences 12, 324. https://doi.org/10.3390/geosciences12090324.

Posamentier, H.W., Allen, G.P., James, D.P., 1992. High resolution sequence stratigraphy – the east Coulee delta. J. Sediment. Petrol. 62, 310–317.

Postma, G., Lang, J., Hoyal, D.C., Fedele, J.J., Demko, T., Abreu, V., Pederson, K.H., 2020. Reconstruction of bedform dynamics controlled by supercritical flow in the

channel–lobe transition zone of a deep-water delta (Sant Llorenç del Munt, northeast Spain, Eocene). Sedimentology 68 (4), 1674–1697.

Rebesco, M., Camerlenghi, A. (Eds.), 2008. Contourites. Elsevier, pp. 1–10.

Rebesco, M., Hernández-Molina, F.J., Van Rooij, D., Wåhlin, A., 2014. Contourites and associated sediments controlled by deep-water circulation processes: state-of-the-art and future considerations. Mar. Geol. 352, 111–154.

Rovida, A., Locati, M., Camassi, R., Lolli, B., Gasperini, P., 2020. The Italian earthquake catalogue CPTI15. Bull. Earthq. Eng. 18 (7), 2953–2984.

Rovida, A., Locati, M., Camassi, R., Lolli, B., Gasperini, P., Antonucci, A. (Eds.), 2022. Italian Parametric Earthquake Catalogue (CPTI15), Version 4.0. Istituto Nazionale di Geofisica e Vulcanologia (INGV). https://doi.org/10.13127/CPTI/CPTI15.4.

Ruello, M.R., Cinque, A., Di Donato, V., Molisso, F., Terrasi, F., Russo Ermolli, E., 2017. Interplay between sea level rise and tectonics in the Holocene evolution of the St. Eufemia Plain (Calabria, Italy). J. Coast. Conserv. 2, 903–915.

Sharp, I.R., Gawthorpe, R.L., Underhill, J.R., Gupta, S., 2000. Fault-propagation folding in extensional settings: examples of structural style and synrift sedimentary response from the Suez rift, Sinai, Egypt. Geol. Soc. Am. Bull. 112 (12), 1877–1899.

Shillington, D.J., Seeber, L., Sorlien, C.C., Steckler, M.S., Kurt, H., Dondurur, D., Cifci, G., Imren, C., Cormier, M.H., McHugh, C.M.G., Gürçay, S., 2012. Evidence for widespread creep on the flanks of the Sea of Marmara transform basin from marine geophysical data. Geology 40 (5), 439–442.

Slootman, A., Cartigny, M.J., 2020. Cyclic steps: review and aggradation-based classification. Earth Sci. Rev. 201, 102949.

Soutter, E.L., Kane, I.A., Hodgson, D.M., Flint, S., 2021. The concavity of submarine canyon longitudinal profiles. J. Geophys. Res. Earth Surf. 126 (10), e2021JF006185.

Tansi, C., Muto, F., Critelli, S., Iovine, G., 2007. Neogene-Quaternary strike-slip tectonics in the central Calabrian Arc (southern Italy). J. Geodyn. 43 (3), 393–414.

Tanyaş, H., van Westen, C.J., Persello, C., Alvioli, M., 2019. Rapid prediction of the magnitude scale of landslide events triggered by an earthquake. Landslides 16 (4), 661–676.

Tertulliani, A., Cucci, L., 2009. Clues to the identification of a seismogenic source from environmental effects: the case of the 1905 Calabria (Southern Italy) earthquake. Nat. Hazards Earth Syst. Sci. 9, 1787–1803. https://doi.org/10.5194/nhess-9-1787-2009.

Tortorici, G., Bianca, M., Monaco, C., Tortorici, L., Tansi, C., De Guidi, G., Catalano, S., 2002. Quaternary normal faulting and marine terracing in the area of Capo Vaticano and S. Eufemia plain (southern Calabria). Studi Geol. Camerti 1, 155–171.

Trincardi, F., Normark, W.R., 1989. Pleistocene Suvero slide, Paola basin, southern Italy. Mar. Pet. Geol. 6 (4), 324–335.

Trincardi, F., Correggiari, A., Field, M.E., Normark, W.R., 1995. Turbidite deposition from multiple sources; Quaternary Paola Basin (eastern Tyrrhenian Sea). J. Sediment. Res. 65 (4b), 469–483.

Trincardi, F., Cattaneo, A., Correggiari, A., Mongardi, S., Breda, A., Asioli, A., 2003. Submarine slides during relative sea level rise: two examples from the eastern Tyrrhenian margin. In: Locat, Jacques, Mienert, Jürgen (Eds.), Submarine Mass Movements and Their Consequences Advances in Natural and Technological Hazards Research, vol. 19. Kluwer Academic Publishers, pp. 469–478.

Van Dijk, J.P., Bello, M., Brancaleoni, G.P., Cantarella, G., Costa, V., Frixa, A., Golfetto, F., Merlini, S., Riva, M., Torricelli, S., Toscano, C., 2000. A regional structural model for the northern sector of the Calabrian Arc (southern Italy). Tectonophysics 324 (4), 267–320.

Watson, S.J., Mountjoy, J.J., Crutchley, G.J., 2020. Tectonic and geomorphic controls on the distribution of submarine landslides across active and passive margins, eastern New Zealand. Geol. Soc. London Spec. Publ. 500, 477–494.

Yokoyama, Y., Lambeck, K., De Deckker, P., Johnston, P., Fifield, L.K., 2000. Timing of the Last Glacial Maximum from observed sea-level minima. Nature 406 (6797), 713–716.